ELSEVIER

Journal of Electron Spectroscopy and Related Phenomena 125 (2002) 221–248

JOURNAL OF ELECTRON SPECTROSCOPY and Related Phenomena

www.elsevier.com/locate/elspec

Review

The hemispherical deflector analyser revisited. I. Motion in the ideal $1/r$ potential, generalized entry conditions, Kepler orbits and spectrometer basic equation

T.J.M. Zouros[a,b,*], E.P. Benis[a,b,1]

[a] *Department of Physics, University of Crete, P.O. Box 2208, 71003 Heraklion, Crete, Greece*
[b] *Institute of Electronic Structure and Laser, P.O. Box 1527, 71110 Heraklion, Crete, Greece*

Received 4 May 2002; received in revised form 14 May 2002; accepted 18 May 2002

Abstract

We re-examine the orbits of non-relativistic charged particles in a hemispherical deflector analyser (HDA) assuming an ideal $1/r$ potential. The particles start their trajectory within the HDA at the arbitrary entry radius $\mathbf{r}_0$, within a circular entry aperture centered at R_0 at an arbitrary potential $V_0 = V(R_0)$. We present a vector treatment of the trajectories deriving many useful relations expressed as a function of the launching angle α. Refraction at the potential boundary at the entry of the HDA (modelled by an idealized step potential) is also considered and found to be important when $V_0 \neq V_p$, where V_p is the plate voltage used for preretardation. We derive the analyser's generalized basic equation for deflection through 180° for which the principal reference ray is an *ellipse* rather than a circle as in the conventional HDA treatment. Both the conventional HDA, for which $R_0 = \bar{R}$ and $V_0 = V_p$, as well as the *paracentric* HDA for which $R_0 \neq \bar{R}$ and $V_0 \neq V_p$, where $\bar{R}$ is the mean radius, are thus described as special cases of the same trajectory equation. Our results are expected to be of interest to all fields of electron spectroscopy, but particularly to those utilizing modern spherical sector analysers with sizeable interradial separation for accommodating large area position-sensitive detectors. This investigation is part of a concerted effort to investigate the refocusing properties of the paracentric HDA recently reported by Benis and Zouros [Nucl. Instr. & Meth. A 440 (2000) 462].

Keywords: Motion in $1/r$ potential; Kepler orbits; Hemispherical analyser; Electron spectroscopy; ESCA; Fringing fields

1. Introduction

In a recent article [1] we demonstrated by ray tracing analysis that the focusing properties of a hemispherical deflector analyser (HDA) [2–6] with a large interradial separation ($\Delta R/\bar{R} \sim 50\%$) depend critically on the placement of the analyser entrance position (entry aperture centered at R_0) and the value of the HDA potential V_0 at R_0. It is well known [7–11] that for HDAs with such large interradial separations, fringing field effects shift the first order focus of an *ideal* HDA, found at a deflection angle of 180°, to smaller angles well inside the HDA [7,9]. This effect is clearly demonstrated by the SIMION

*Corresponding author. Tel.: +30-81-394-117; fax: +30-810-394-101.
E-mail address: tzouros@physics.uoc.gr (T.J.M. Zouros).
[1] Present address: J.R. Macdonald Laboratory, Kansas State University, Manhattan, KS 66506-2604, USA.

0368-2048/02/$ – see front matter
PII: S0368-2048(02)00137-8

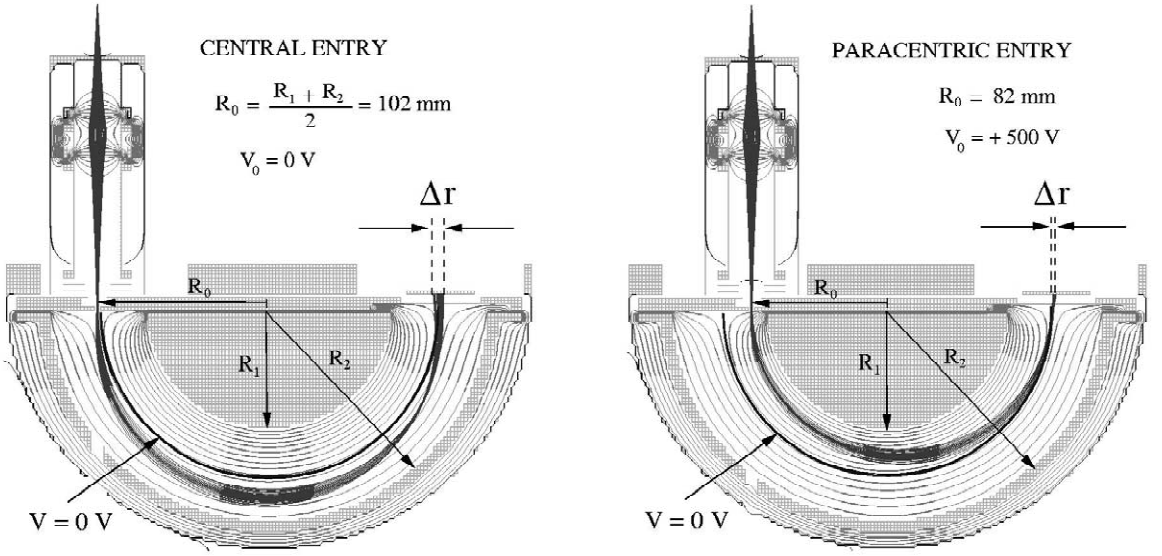

Fig. 1. SIMION simulation of HDA with parameters given by Table 1. Electrons within an emittance cone angle of 6° are flown through a lens and focused into an HDA with a principal ray pass energy of $w = 1000$ eV. The voltages on the HDA are the *same* in both cases and set according to Eq. (109) using $R_0 = \bar{R} = R_\pi = 102$ mm and $V_0 \equiv V(R_0) = 0$ V. [Left] central entry with $R_0 = 102$ mm. The focus point is seen to have moved inside the spectrometer resulting in a wide trace Δr in the 180° detection plane. [Right] Entry and lens were moved to $R_0 = 82$ mm in the vicinity of which SIMION shows $V(82\text{ mm})$ to be approximately 500 V. The first order focus is seen to be restored back to the 180° detection plane reducing the width of the trace Δr. Equipotential lines show the strong fringing fields at both entry and exit. The entry radius at which the focus is restored is shown in Ref. [1] to be a function of V_0, the nominal potential at entry.

[12] simulation of Fig. 1 (left). This shift results in a badly focused image at the 180° detection plane adversely affecting the energy resolution of the HDA (see Fig. 1 left). It was shown in Ref. [1] that for particular combinations of R_0 ($< \bar{R}$) and V_0 the focus *can be shifted back* to the 180° detection plane, practically restoring the 180° first order focusing properties of the HDA (see Fig. 1 right) *without* the use of any additional fringing field correction scheme [11,13–26].

This rather remarkable property of the *non-ideal* paracentric HDA, seemingly unnoticed in almost 60 years of intense HDA development, should be of particular interest to all fields utilizing modern high resolution HDAs, having sizeable interradial separations for accommodating large area position sensitive detectors for high detection efficiency. Particularly so, if cumbersome fringing field electrodes can be shown not to be necessary.

We are presently using such a paracentric HDA [27–29] with parameters as given in Table 1 operated with a four-element zoom lens and a 2-D position sensitive detector (PSD). This HDA has an entry aperture centered at $R_0 = 82.55$ mm with diameter $d_i = 6$ mm and is operated with $V_0 = 0.5w$, where w is the nominal tuning energy. A FWHM resolution of ~0.11% has been attained using pre-retardation by a factor $F = 8$ without the use of any fringing field correction electrodes. The spectrograph is used to study the excitation mechanisms of highly

Table 1
Paracentric HDA parameters

R_1	72.4 mm	inner radius
R_0	82.55 mm	principal ray entry radius
R_2	130.8 mm	outer radius
$\bar{R}$	101.6 mm	mean radius
R_π	$\bar{R}$	principal ray exit radius
d_{PSD}	40 mm	active PSD diameter
d_i	6 mm	diameter of entry aperture centered on R_0
V_0	$0.5w$	nominal voltage at $V(R_0)$
γ	1.5	see Eq. (3)
ξ	1.2308	$= \frac{R_\pi}{R_0}$

charged ions in atomic collisions with gas targets using the technique of Zero-degree Auger electron Projectile Spectroscopy (ZAPS) [30].

To use our paracentric HDA, we had to derive the spectrometer basic equation from first principles for the *ideal* HDA [31] since no such treatment was found in the literature. To further understand the *real* HDA, the effects of the strong fringing fields were investigated by simulation using the ion-optics software package SIMION [12]. The refocusing of the particle trajectories back onto the 180° image plane has already been briefly described [1]. Here, we give a more detailed presentation in a series of three papers, providing further insight into this refocusing effect, while at the same time giving a brief up-to-date review of the field.

In this paper (paper I) we present details about Kepler orbits (i.e. closed trajectories in an *ideal* $1/r$ potential). We first derive the trajectory equations $r(\omega)$ (ω is the deflection angle in the orbital plane) for arbitrary entry R_0 and V_0 including the effect of charged particle refraction at the HDA entry potential boundary, usually ignored in conventional HDA treatments, but here shown to be a non-negligible effect. Such a generalized treatment requires the use of an *elliptical* principal reference ray rather than the *circular* one traditionally used in most conventional applications [2,4–6,32,33]. This does not alter the known double focusing properties of the ideal HDA, but shows that the refocusing effects in a real paracentric analyser is clearly due to the fringing fields at the entry and exit of the HDA. We then obtain the basic equation of the ideal spectrograph which relates the exit position r_π in the first order focusing plane to the entrance position r_0 as a function of entry energy and angle. From this equation we also derive the electrode voltages necessary for its operation. We develop many useful formulas and discuss some interesting properties of Kepler orbits related to the ideal HDA's first order focusing properties. In the appendices much of the details of the various derivations are given. In Appendix A a convenient list of symbol definitions is given.

In a follow-up paper (paper II) [34], we use the basic spectrometer equation derived in I to investigate the operation and optical properties of the *ideal* HDA. These include dispersion, energy resolution, optimum lens magnification, energy calibration, energy acceptance window and time-of-flight. We then compare these results to SIMION simulations and experimental measurements taken with our paracentric HDA, thus also including possible effects due to the strong fringing fields at the entrance and exit.

Finally, in paper III [35], we compare particle trajectories to simulations obtained with SIMION for motion including the effect of the fringing fields for both conventional and paracentric cases. Basic trajectory parameters (position, velocity, electric fields, kinetic and potential energy, etc.) that change along the trajectory are compared for motion in the ideal $1/r$ and in the strong fringing fields of the SIMION simulated HDA. A much better insight is obtained on the importance of the fringing fields and their focusing properties.

In our presentation (papers I–III), the conventional HDA is just a special case of the more general paracentric HDA directly obtained for $R_0 = R$ and $V_0 = V_p$. In each paper we present a brief history of relevant results and investigations to date.

2. Definitions and basic considerations

The schematic of the HDA model under study is shown in Fig. 2. The spherical polar coordinate system (r, θ, ϕ) centered at O is adopted to take advantage of the rotational symmetry of the HDA around $\theta = 0$ (Z-axis). The analyser consists of two concentric hemispherical plates of inner and outer radii R_1 and R_2, respectively. The center of the hemispheres is set as the origin of the coordinate system. The paracentric entry is located at distance R_0, while a PSD is placed at the HDA exit centered at distance $R_\pi \equiv R = (R_1 + R_2)/2$. The use of such a PSD allows for the detection of a whole energy range of particles simultaneously, reducing substantially the acquisition time of the spectrum. A cylindrical lens system is mounted with its optical axis centered at the paracentric entry for focusing and deceleration purposes. A particle of charge q, mass m and initial kinetic energy T is ejected at *zero* potential far from the spectrograph. Prior to entering the analyser it passes through the deceleration/focus-

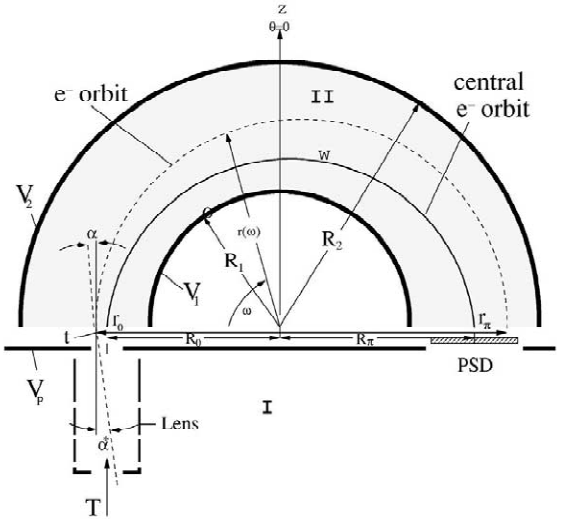

Fig. 2. Schematic of HDA geometry. The charged particle initially enters the lens assembly with kinetic energy T and is then focused and decelerated by the lens and plate at potential V_p down to an energy t just prior to entering the interior region (region II see text) of the analyser (shaded area) with angle α^*. The deflection angle in the plane of the orbit is ω. Upon crossing the sharp (step-potential model) potential boundary at $\theta = \pi/2(\omega = 0)$ at $r_0$and potential $V(r_0)$, it is refracted to an angle α, follows the trajectory specified by $r(\omega)$and exits at r_π after being deflected through an angle π. The center of the entrance aperture is paracentric at $R_0 < R$. Fixing the principal trajectory ($\alpha^* = 0$) to an *ellipse* such that for $t = w$ and $r_0 = R_0$ the exit occurs at $r_\pi = R\pi$, fixes the analyser voltages.

ing stage which can change its kinetic energy to t such that:

$$t = T - qV_p \tag{1}$$

by applying a potential V_p on the last electrode of the deceleration stage. Electrons ($q = -e$) are typically decelerated to improve their energy resolution [36–40] by applying a negative V_p. When deceleration is not required, V_p is set to zero ($V_p = 0$).

The potential $V(r, \theta, \phi)$ is expected to have azimuthal symmetry with the generic form given by $V(r, \theta) = \Sigma_l f_l(r, R_1, R_2)P_l(\cos\theta)$ [41,42] with $V(R_1) = V_1$ and $V(R_2) = V_2$ specifying the boundary conditions. In our theoretical analysis to follow (paper I) it is assumed that *inside* the HDA we have an *ideal* $1/r$ potential, given by:

$$V(r, \theta) = V(\tilde{r}) = \tilde{V}(r) + V_p \tag{2}$$

where $\tilde{V}(r) = -k/r + c$. The symbols $V_1 \equiv V(R_1)$, $V_2 \equiv V(R_2)$ and the corresponding $\tilde{V}_1$, $\tilde{V}_2$ are reserved for the inner and outer hemispheres, respectively. Also the symbol $V_0 \equiv V(R_0)$ and the corresponding $\tilde{V}_0$ is reserved for the value of the potential at the center of the entry aperture at R_0. We note that our voltage definitions give the *actual* voltages applied to the electrodes as supplied by the high voltage power supplies which are referenced to ground.

The particle enters the HDA crossing the $\theta = \pi/2$ boundary plane at a point $\mathbf{r}_0$ (within the entrance aperture centered at R_0) with kinetic energy t, polar angle α and azimuthal angle β. The angular momentum $\mathbf{L}$ is conserved as is well-known for motion in a central potential and thus the trajectory will lie in a plane perpendicular to $\mathbf{L}$. Thus, β just rotates the motional plane around the axis defined by the entrance point r_0 and the center of the analyser (see Fig. 3). The particle then follows a trajectory specified by $r(\omega)$, where ω is the deflection angle within the orbital plane, and exits at $\mathbf{r}_\pi$ after being deflected through $\Delta\omega = \pi$.

In a conventional HDA, $V_0 = V_p$ and thus the particle entering at r_0 will not feel any substantial change of kinetic energy in going from V_p to $V(r_0)$, since the variation between $V(r_0)$ and $V(R_0)$, will in general be small within the limited diameter of the spectrometer's aperture. Furthermore, in a conventional HDA, the *principal* ray (particle entering with kinetic energy $t = w$, $\alpha = 0$ and $r_0 = r_\pi = R$) will describe a circular trajectory and go through the HDA with the *constant* pass energy w. Similarly, in a paracentric HDA with, however, $V_0 = V_p$, the principal ray ($t = w$, $\alpha = 0$ and $r_0 = R_0$, $r_\pi = R_\pi$) will also not feel any large change in its kinetic energy at entry. However, since $R_0 \neq R_\pi$ (e.g. it is required to exit at a different radius) it will necessarily follow an elliptical trajectory and its pass energy will therefore *not* be constant.

However, when V_0 is substantially different from V_p, then in both cases above, the particle is refracted and its kinetic energy at entry changes. If we define the parameter γ so that:

$$q(V_0 - V_p) = q\tilde{V}_0 \equiv (1 - \gamma)w \tag{3}$$

then any *principal* ray will be *accelerated* when $q(V_0 - V_p) < 0$ ($\gamma > 1$) to a new energy $w' = \gamma w$.

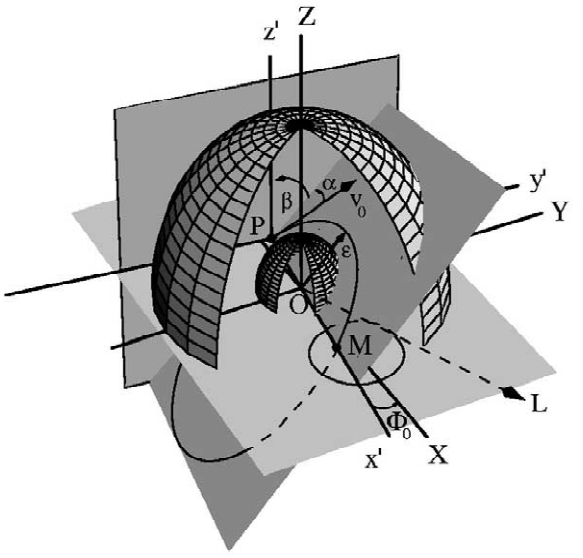

Fig. 3. A 3-D orbit in an HDA obtained with the use of Eq. (60). Charged particle enters at P ($X_0 = -78.6$, $Y_0 = 10$, $Z_0 = 0$) and exits at M ($X_\pi = 86.6$, $Y_\pi = -11.0$, $Z_\pi = 0$) with $\alpha^* = -30°(\alpha = -23.84°)$, $\beta = -50°$, $\gamma = 1.5$, $t = 1160$ eV and $w = 1000$ eV ($\tau = 1.16$). Definitions of angles α, β and Φ_0 are clearly shown. Note in this figure α, β and Φ_0 are actually negative following traditional sign convention [43,44]. The laboratory coordinate system **XYZ** is centered on the analyser center at O, while the relative coordinate system $x'y'z'$ is centered at particle entry point P with both XY and $x'y'$ planes identical corresponding to $Z = z' = 0$. The $x'y'$ axes are rotated by $\Phi_0 = -7.26°$ with respect to the fixed XY axes. Angle β is measured off the z'-axis in the $x' = 0$ plane which is perpendicular to the nodal line POM (intersection of orbit plane and $Z = 0$ plane) which also lies along the entry position vector $\mathbf{r}_0$(OP). Angle α is measured off the intersection of the orbit plane with the $x' = 0$ plane in the direction of v_0. Thus, the plane $x' = 0$ and the orbit plane are mutually perpendicular. Exit point M also lies in the $Z = 0$ plane and corresponds to a deflection by π in the plane of the orbit. Also shown are the entry velocity v_0 and the conserved eccentricity vector $\boldsymbol{\epsilon}$ and angular momentum vector $\mathbf{L}$. The length of $\boldsymbol{\epsilon}$ has been renormalized to r_{min} for better viewing. The radius of the inner hemisphere is shown for clarity much smaller than its actual size. The outer radius is shown to scale. For the calculation we have used the parameters of Table 1.

We shall preserve the use of the term, 'pass energy' w, to describe the kinetic energy of the particle just prior to entry, even though as shown it is not anymore constant through out its motion within the HDA in the more general case of a paracentric HDA. This, nominal pass-energy w will also be referred to as the analyser *tuning energy* [45], since only electrons within a certain energy acceptance window around w will be analysed. For analysing systems with deceleration, as in the present case, one may also define an 'undecelerated tuning energy' W (using Eq. (1)):

$$W \equiv w + qV_p \tag{4}$$

and the deceleration ratio F:

$$F \equiv \frac{W}{w} \tag{5}$$

so that a principal ray with kinetic energy W far from the spectrometer (at 'infinity') undergoing deceleration with factor F will have the energy w just prior to entering the HDA. The 'reduced' pass energy τ is also defined as:

$$\tau \equiv \frac{t}{w} = F\left(\frac{T}{W} - 1\right) + 1 \tag{6}$$

expressed also in terms of the undecelerated quantities, T, W and deceleration factor F. Finally, we shall also introduce the parameter ξ, characterizing the 'asymmetry' of the HDA:

$$\xi \equiv \frac{R_\pi}{R_0} \tag{7}$$

A conventional HDA is seen to have $\xi = 1$ and $\gamma = 1$.

Given that particles are usually decelerated to improve their detected energy resolution [36–40], it seems particularly surprising that a device which would re-accelerate particles once inside the dispersive medium could be of any practical interest. In principle, such a re-acceleration can only be expected to degrade the analyser resolution, annulling the beneficial effects of the prior deceleration. However, on the positive side, dispersion at a higher pass energy will increase the energy acceptance window of the HDA thus providing increased throughput and will also desensitize, to some extent, the energy analysis from the deleterious effects of spurious magnetic and electric fields usually of great concern when working at low electron pass energies. It will also lead to smaller time-of-flights with compressed time distributions also an advantage in coincidence work. That such a paracentric HDA can in fact also improve the energy resolution, as we recently dem-

onstrated in an ion-optics simulation [1], is certainly unexpected.

3. Motion in an ideal $1/r$ potential

3.1. Earlier work on HDAs

The study of the trajectories of particles in a $1/r$ potential is a well known field in classical mechanics treated as a special section in all standard classical mechanics textbooks under motion in a central field (see for example Refs. [46–48]). However, since the emphasis in classical mechanics is primarily on planetary motion, special aspects having to do with the focusing of charged particles and its dependence on the launching angles α and β are not usually treated. The advent of modern satellites with their deployment for commercial and military purposes in outer space has brought new interest to the field with a change of emphasis in new text books (see for example Ref. [49]). We shall adapt the treatment of Ref. [49] for the development of HDA trajectory investigations.

Many good reviews have been published in the past on electrostatic spectrometers in general, including to some extent trajectory theory, the most recent to our knowledge by Roy and Tremblay [50]. There are also many excellent books on charged particle optics in general (see for example Ref. [22]) as well as more specific books on electron spectroscopy that cover much useful material (see for example Ref. [51]). Some older but very useful reviews on HDAs and dispersive devices in general include Refs. [32,52–57].

Purcell [2] was the first to study the trajectories of charged particles traversing a portion of an ideal $1/r$ potential, to demonstrate its special focusing properties and to actually construct a spherical condenser for use in electron spectroscopy. Ever since, the hemispherical version of the spherical condenser has become extremely popular—primarily due to its double focusing properties, its large luminosity [58] and rugged construction—in electron spectroscopy, and many HDAs have been studied and utilized in experiments covering many fields of applications including most of atomic and molecular physics, condensed matter physics and surface science.

Kuyatt and Simpson [4] developed an electron monochromator based on an HDA. The choice of the slit width and electron energy at a given energy resolution for maximum current were investigated in their paper. Their choice of equal size entrance and exit round entrance apertures instead of slits, with dimensions satisfying the restriction $\alpha^2 \leq d_i/(4\bar{R})$ (where α is the pencil angle, w the aperture diameter and $\bar{R}$ the analyser mean radius) became the standard criteria for HDA design. Paolini and Theodoridis [43] and Kemeny et al. [59] developed some of the early theory and reported on the transmission properties of spherical plate electrostatic analysers. Wollnik [22,52] investigated the trajectories of charged particles in electrostatic toroidal condensers including the effect of refraction and fringing field corrections on their motion. Roy and Carette [32,60] included the hemispherical spectrometer in their method of calculating the energy distribution of electrons selected electrostatically. They presented some of the first detailed work on the trajectory equations which are obtained as a special case of the more general motion in a toroidal spectrometer treated by Wollnik [14,52,61]. Refraction at the potential boundary, however, is ignored. It is included later though in the study of the optimization of the HDA by Poulin and Roy [62]. Heddle [58] reported on the comparison of the *étendue* of electron spectrometers including HDA's. Chase [42] investigated the effects of the fringing fields on the HDA response function in an HDA with large interradial separation in a numerical perturbation calculation. Polaschegg [38] reported on the features of the spherical analysers with and without preretardation. He also reported on the study of the energy resolution and the intensity behavior of spherical analysers as a function of the entrance parameters [63]. Sköllermo and Wannberg [17] gave a detailed description of the influence of fringing fields on the focusing properties of HDAs. They first numerically calculated the electrostatic potential of an HDA by solving Laplace's equation and then investigated the effects of the calculated fringing fields on the electron trajectories and the focussing effects of the HDA. Imhof et al. [64] studied the energy resolution and transit time spread in hemispherical analysers involved in coincidence experiments. Draper and Ulloa [33] provided some useful insight into the properties of Kepler orbits and their dependence on the launching conditions. Some of

their results are also used in our presentation. They do also treat the potential discontinuity at entry and discuss to some extent the effect of fringing fields and the Herzog correction scheme [13]. Kevan [5] reported on design criteria for a high-resolution angle-resolving HDA. Hadjarab and Erskine [6] reported on the imaging properties of an HDA used with a position sensitive detector (PSD), replacing in this way the commonly used exit slit with a large area detector. Trajectory equations for conventional HDAs are also obtained from first principles and refraction at the potential boundary is also treated. Boesten [65] investigated the shape and extent of space-charge in an analytical treatment of the trajectory parameters in an 180° spherical monochromator. Nishigaki and Kanai [7] studied the effects of the fringing fields on the trajectories in a numerical calculation and showed that the focusing of a real HDA is shifted to deflection angles within the HDA ($\Delta\omega < 180°$). They also showed how this could be improved by optimizing the Herzog correction. A double-stage spectrograph consisting of two HDAs is reported by Mann and Linder [66], and Baraldi and Dhanak [67] giving trajectory equations which include the effect of refraction. Page and Read [68] investigated the energy non-linearity of an HDA when used with a large area multi-detector anode or PSD and showed that the fringing fields at the exit, when left uncorrected, lead to improved energy linearity if the detection plane is shifted slightly out of the HDA. Thus, it is shown that fringing fields may even have beneficial effects under certain conditions. Finally, in Benis and Zouros [1], a way to use the fringing fields to improve HDA resolution is empirically found using SIMION simulation.

In the past 30 years since the early days of ESCA [69], increased interest has focused on HDAs used with large position sensitive detectors (PSD) in such diverse fields as surface analysis, e−2e measurements, photoelectron spectroscopy and various measurements involving synchrotron radiation. These spectrometers have also become of great commercial interest as there are numerous high-tech companies increasingly selling expensive state-of-the-art devices with FWHM energy resolutions of 2 meV or less and capable of data acquisition rates around 1 MHz and more.

All studies to date, have basically treated the specific case of a hemispherical spectrometer constructed with the center of entry and exit apertures placed at the mean radius of the analyser opening (i.e. $R_0 = \bar{R} = (R_1 + R_2)/2$) at a potential $V_0 = V_p$ (see Fig. 2). In this conventional HDA arrangement the principal ray is a *circle*. Recently, however, some analysers whose exit, due to space limitations, could not be placed at $\bar{R}$ have been reported in the literature [70].

In this work (paper I), the more general case of an HDA with entry at an arbitrary radius R_0 and potential V_0 is studied in detail. R_0 and V_0 are considered as free parameters of the trajectory motion which can be varied to investigate the general focusing and dispersive properties of the HDA. The generalized trajectory equations are compared to well-known results from the literature, which arise as special solutions to our more general results. Thus, both the conventional HDA ($R_0 = \bar{R}$, $V_0 = V_p$) and the paracentric HDA ($R_0 \neq \bar{R}$, $V_0 \neq V_p$) are described within the same analysis.

In our theoretical study, the electrostatic field is considered ideal, i.e. fringing field effects, primarily present at the HDA entry and exit, are not taken into account. However, for HDAs used with large PSDs, fringing field effects become important, resulting in departures from the spectrograph properties predicted for ideal fields theoretically. In the literature, different schemes for treating the fringing field effects have been reported [6,7,11,13,19,25,41,42,68,71]. We shall be particularly concerned with the effects of the fringing fields in papers II and III.

3.2. General trajectory equations

The trajectory of a charged particle in an $1/r$ potential has been presented in the literature (see for example Refs. [2,6,32,43] for spherical sectors and Refs. [14,52,72,73] for toroidal sectors). Here we present a comprehensive treatment using vector formalism [49] and we also explicitly include refraction effects usually not included (for exceptions see Refs. [2,6,14,25,64,66]).

The classical, non-relativistic equations of motion for a particle of mass m and charge q in the potential $\tilde{V}(r, \theta)$ are given by:

$$m\ddot{\mathbf{r}} + q\nabla\tilde{V}(r, \theta) = 0 \tag{8}$$

Assuming an ideal $1/r$ potential for the region *inside*

the HDA of the form $\tilde{V}(r,\theta)=\tilde{V}(r)=-k/r+c$ we get:

$$\ddot{\mathbf{r}}+\frac{qk}{m}\frac{\mathbf{r}}{r^3}=0 \quad \text{for} \quad 0\le\theta<\frac{\pi}{2} \tag{9}$$

It is seen from Eq. (9) that the constant c does not enter the equations of motion *inside* the HDA. As will be shown in the next section it is only used to match the boundary conditions at $\theta=\pi/2$. The potential constants k and c will be fixed later through the definition of the principal reference trajectory. We retain the charge of the particle q (for electrons $q=-e$) for generality.

The angular momentum inside the HDA, $\mathbf{L}\equiv\mathbf{r}\times m\mathbf{v}=\mathbf{r}\times m\dot{\mathbf{r}}$ is conserved for any central potential $V(r)$ and therefore motion is confined to a plane.

To solve Eq. (9) we take the cross product with $\mathbf{L}$:

$$\ddot{\mathbf{r}}\times\mathbf{L}=-\frac{qk}{mr^3}\mathbf{r}\times\mathbf{L}=-\frac{qk}{r^3}\mathbf{r}\times(\mathbf{r}\times\dot{\mathbf{r}}) \tag{10}$$

$$=\frac{qk}{r^3}[\dot{\mathbf{r}}r^2-\mathbf{r}(\mathbf{r}\cdot\dot{\mathbf{r}})] \tag{11}$$

$$=qk\left[\frac{\dot{\mathbf{r}}}{r}-\frac{\mathbf{r}\dot{r}}{r^2}\right] \tag{12}$$

where we have used the vector identities $A\times(B\times C)\equiv B(A\cdot C)-C(A\cdot B)$ and $\frac{1}{2}\,\mathrm{d}/\mathrm{d}t(\mathbf{r}\cdot\mathbf{r})\equiv\mathbf{r}\cdot\dot{\mathbf{r}}=r\dot{r}$.

Noting that

$$\frac{\mathrm{d}}{\mathrm{d}t}\left(\frac{\mathbf{r}}{r}\right)=\frac{r\dot{\mathbf{r}}-\mathbf{r}\dot{r}}{r^2} \tag{13}$$

we can write Eq. (12) as

$$\frac{\mathrm{d}}{\mathrm{d}t}\left(\dot{\mathbf{r}}\times\mathbf{L}-qk\frac{\mathbf{r}}{r}\right)=0 \tag{14}$$

which upon integration gives us a new *vector* constant of the motion $\boldsymbol{\epsilon}$ [49,74]:

$$\boldsymbol{\epsilon}\equiv\frac{\dot{\mathbf{r}}\times\mathbf{L}}{qk}-\frac{\mathbf{r}}{r}=\text{constant} \tag{15}$$

It is seen that $\boldsymbol{\epsilon}$ is proportional to the Runge–Lenz vector $\mathbf{A}=qk\boldsymbol{\epsilon}$ [47] known to be *conserved* for motion in a $1/r$ potential. Clearly, $\boldsymbol{\epsilon}$ lies in the orbital plane since from Eq. (15) it is seen to be perpendicular to the angular momentum $\mathbf{L}$.

Taking the dot product of $m\mathbf{r}$ with Eq. (15) and using the vector identity $\mathbf{A}\cdot(\mathbf{B}\times\mathbf{C})\equiv\mathbf{C}\cdot(\mathbf{A}\times\mathbf{B})$ obtaining the equality $m\mathbf{r}\cdot(\dot{\mathbf{r}}\times\mathbf{L})=L^2$, eliminates the dependence on $\dot{\mathbf{r}}$ yielding the scalar equation of motion for r:

$$r_\omega\equiv r(\omega)=r=\frac{p}{1+\hat{\mathbf{r}}\cdot\boldsymbol{\epsilon}} \tag{16}$$

$$=\frac{p}{1+\epsilon\cos(\omega-\omega_\epsilon)} \tag{17}$$

with

$$p\equiv\frac{L^2}{mqk} \tag{18}$$

Eq. (17) is seen to be the well-known equation of a conic section in polar coordinates with the origin of the coordinate frame at the focus of the conic section and *latus rectum* p [46–48]. For $0<\epsilon<1$, the orbit is an ellipse with eccentricity $\epsilon=|\boldsymbol{\epsilon}|$. For $\epsilon=0$ the orbit is a circle with radius p, while for $\epsilon=1$ the orbit is a parabola. When $\epsilon>1$, the orbit is a hyperbola [46,48]. The angle $\omega-\omega_\epsilon$ is just the angle between the two vectors $\mathbf{r}$ and $\boldsymbol{\epsilon}$. When $\omega=\omega_\epsilon$, it is seen that r is a minimum and thus $\boldsymbol{\epsilon}$ has the useful property that it *always points to periapse*. In the case of an ellipse, the general form given by Eq. (17) is shown in Fig. 4 (left) for an arbitrary coordinate system xy.

Taking the dot product of $\boldsymbol{\epsilon}$ with itself in Eq. (15) we obtain the well known relation:

$$\epsilon=\sqrt{1+\frac{2EL^2}{mq^2k^2}} \tag{19}$$

with

$$E=\frac{1}{2}mv^2-\frac{qk}{r} \tag{20}$$

where $v=|\dot{\mathbf{r}}|$ is the speed of the particle. Since both L and $\boldsymbol{\epsilon}$ are conserved, Eq. (19) shows that E must also be conserved, making it the *effective* total energy within the analyser. When E is negative, $\boldsymbol{\epsilon}$ is seen to be smaller than 1 and the quantity $1+\epsilon\cos(\omega-\omega_\epsilon)$ in Eq. (17) can never be zero leading in general to bound elliptical orbits.

We also introduce the velocity angle in the orbital plane, α_ω, (see also Figs. 4 and 7) so that:

$$\mathbf{v}\cdot\mathbf{r}=vr\sin\alpha_\omega \tag{21}$$

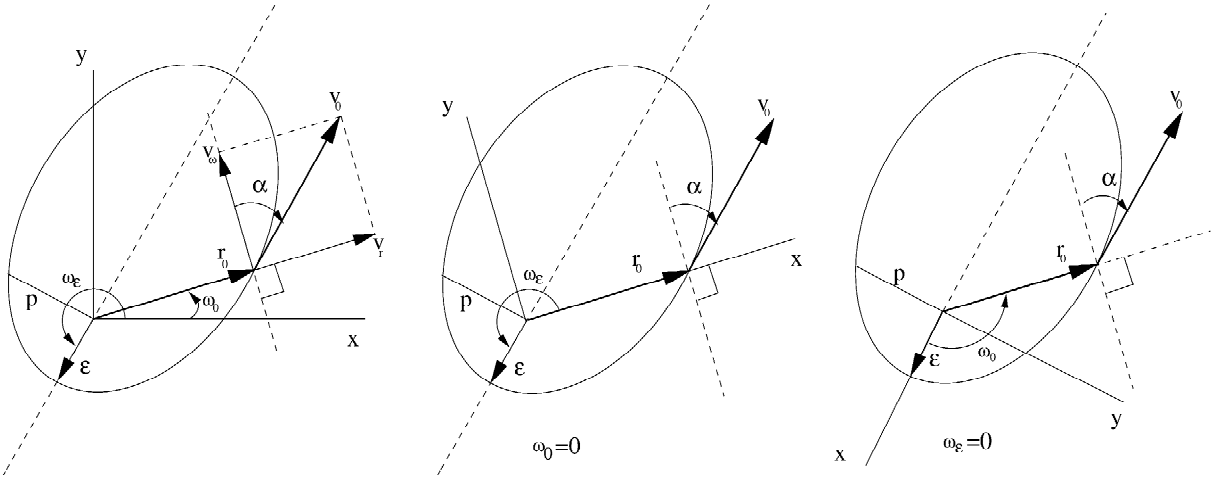

Fig. 4. Elliptical orbits in different coordinate systems. The eccentricity vector $\boldsymbol{\epsilon}$ always points to r_{min} or periapse. For improved viewing it is shown here with length r_{min}. Also shown is the latus rectum p and the position and velocity vectors at *entry* $\mathbf{r}_0$, v_0 and angle α. For $\alpha > 0$, *r always increases* (particle moves away from periapse), while for $\alpha < 0$, *r always decreases* (particle moves towards periapse). *xy* coordinate systems: (left) arbitrary, (center) with $\omega_0 = 0$ and (right) with $\omega_\epsilon = 0$.

Then, in the orbital plane where $\mathbf{v} = v_r\hat{\mathbf{r}} + v_\omega\hat{\boldsymbol{\omega}}$ we have:

$$v_\omega \equiv v\cos\alpha_\omega \tag{22}$$

$$\equiv r\dot{\omega} = \frac{L}{mr} \tag{23}$$

and

$$v_r \equiv v\sin\alpha_\omega \tag{24}$$

$$\equiv \dot{r} = \frac{v_\omega}{r}\frac{\partial r}{\partial\omega} \tag{25}$$

$$= \frac{qk\epsilon}{L}\sin(\omega-\omega_\epsilon) \tag{26}$$

with $|\alpha_\omega| < \pi/2$. We retain the traditional [43,44] symbol α for the angle α_0 at entry $\omega = \omega_0$ (i.e. $\alpha \equiv \alpha_0$—see Fig. 4). Eqs. (22) and (24) conform to the usual sign convention for α [32,44]. We note that in realistic HDA usage α is rarely larger than 10° and usually smaller than 1°.

The speed v is obtained directly from Eq. (20):

$$v = |\mathbf{v}| = \sqrt{\frac{2\left(E+\frac{qk}{r}\right)}{m}} \tag{27}$$

In deriving the expression for v_r (Eq. (26)) we have used the relation:

$$\frac{\partial r}{\partial\omega} = \frac{\epsilon}{p}\sin(\omega-\omega_\epsilon)r^2 \tag{28}$$

readily obtained from the identity

$$\frac{\partial}{\partial\omega}\left(\frac{1}{r}\right) \equiv \frac{\partial}{\partial r}\left(\frac{1}{r}\right)\frac{\partial r}{\partial\omega} = -\frac{1}{r^2}\frac{\partial r}{\partial\omega}$$

$$= -\frac{\epsilon}{p}\sin(\omega-\omega_\epsilon) \tag{29}$$

and direct differentiation of the equation of motion Eq. (17).

Finally, a very useful property of the orbit [33] can be obtained making use of Eqs. (22), (24) and (25):

$$\tan\alpha_\omega = \frac{v_r}{v_\omega} = \frac{1}{r}\frac{\partial r}{\partial\omega} \tag{30}$$

$$= \frac{\epsilon}{p}\sin(\omega-\omega_\epsilon)r \tag{31}$$

This information is particularly useful for visualizing the orbit. At entry where for $\alpha < 0$ (or $\omega_0 - \omega_\epsilon < 0$), Eqs. (30) and (31) show that $\partial r/\partial\omega < 0$ and therefore the particle is moving towards decreasing r (i.e. towards the periapse to which $\boldsymbol{\epsilon}$ is pointing to), while

for $\alpha > 0$ (or $\omega_0 - \omega_\epsilon > 0$) the particle is moving away from periapse [33]. We may also obtain the relation between the launching angle at entry α and the exit angle α_π after deflection by 180°:

$$\tan\alpha_\pi = -\frac{r_\pi}{r_0}\tan\alpha \tag{32}$$

3.3. Initial conditions

To further define the trajectory we need to specify the conserved energy E, angular momentum L and direction of $\boldsymbol{\epsilon}$ (ω_ϵ). This can be done using the initial values of position $\mathbf{r}_0$ and velocity v_0 of the analysed particle specified at the entrance of the spectrometer in the plane of the orbit (see Fig. 4):

$$\mathbf{r}_0 = \mathbf{r}(r_0, \omega_0) \tag{33}$$

$$\mathbf{v}_0 = \mathbf{v}(v_0, \alpha_0) \equiv \mathbf{v}(v_0, \alpha) \tag{34}$$

$$\mathbf{L} = m\mathbf{r}_0 \times \mathbf{v}_0 \tag{35}$$

$$L = |\mathbf{L}| = mr_0 v_0 \cos\alpha \tag{36}$$

$$E = \frac{1}{2}mv_0^2 - \frac{qk}{r_0} \tag{37}$$

$$\boldsymbol{\epsilon} = \frac{\dot{\mathbf{r}}_0 \times \mathbf{L}}{qk} - \frac{\mathbf{r}_0}{r_0} \tag{38}$$

The eccentricity ϵ and latus rectum p can be written directly in terms of initial condition quantities as:

$$p = 2r_0\left(1 - \frac{r_0}{2a}\right)\cos^2\alpha \tag{39}$$

$$\epsilon = \sqrt{\sin^2\alpha + \left(1 - \frac{r_0}{a}\right)^2\cos^2\alpha} \tag{40}$$

where we have introduced the α-independent quantity a:

$$a \equiv -\frac{qk}{2E} \tag{41}$$

known to be the *semi-major axis* in the case of elliptical motion.

The eccentricity vector $\boldsymbol{\epsilon}$ can also be written as:

$$\boldsymbol{\epsilon} = \hat{\mathbf{r}}_0\left(1 - \frac{r_0}{a}\right) - 2\hat{\mathbf{v}}_0\left(1 - \frac{r_0}{2a}\right)\sin\alpha \tag{42}$$

explicitly showing that its direction depends on the sign of α, while its magnitude (Eq. (40)) does not.

Finally, to completely specify the elliptical trajectory we also need to determine the angular quantity $\omega_0 - \omega_\epsilon$ appearing in Eq. (17). This is the angle with respect to periapse at which the particle starts its trajectory as seen in Fig. 4. This can be directly obtained from the initial conditions using Eqs. (31) and (17):

$$\sin(\omega_0 - \omega_\epsilon) = \frac{p}{\epsilon r_0}\tan\alpha \tag{43}$$

$$= \frac{2\left(1 - \frac{r_0}{2a}\right)\sin\alpha\cos\alpha}{\sqrt{\sin^2\alpha + \left(1 - \frac{r_0}{a}\right)^2\cos^2\alpha}} \tag{44}$$

$$\cos(\omega_0 - \omega_\epsilon) = \frac{\frac{p}{r_0} - 1}{\epsilon}$$

$$= \frac{2\left(1 - \frac{r_0}{2a}\right)\cos^2\alpha - 1}{\sqrt{\sin^2\alpha + \left(1 - \frac{r_0}{a}\right)^2\cos^2\alpha}} \tag{45}$$

$$\tan(\omega_0 - \omega_\epsilon) = \frac{\tan\alpha}{1 - \frac{r_0}{p}} \tag{46}$$

$$= \frac{2\left(1 - \frac{r_0}{2a}\right)\sin\alpha\cos\alpha}{2\left(1 - \frac{r_0}{2a}\right)\cos^2\alpha - 1} \tag{47}$$

A useful constant is ϵ/p which can be easily shown from Eq. (43) to be:

$$\frac{\epsilon}{p} = \frac{\tan\alpha}{r_0\sin(\omega_0 - \omega_\epsilon)} \tag{48}$$

Using Eqs. (39), (45) and (48), the ellipse of Eq. (17) may finally be written as:

$$\frac{r_0}{r_\omega} = \frac{a}{(2a - r_0)\cos^2\alpha} + \frac{\tan\alpha}{\sin(\omega_0 - \omega_\epsilon)}\cos(\omega - \omega_\epsilon) \tag{49}$$

thus expressing the orbit in terms of the initial value quantities r_0, v_0 (via a), and angles α, $\omega_0 - \omega_\epsilon$. We note that both ω_0 and ω_ϵ are functions of the entry angle α. However, since only the difference $\omega_0 - \omega_\epsilon$ is required we may chose $\omega_0 = 0$ or $\omega_\epsilon = 0$ at our

convenience by choosing an appropriate coordinate system *xy* as shown in Fig. 4.

To fully determine the orbits we still need to specify the potential constants *qk* and *qc*. This is usually done by setting the voltages on the HDA in such a way that the principal ray ($\alpha = 0$, $r_0 = R_0$) with energy $t = w$ will exit at a convenient radius R_π, usually chosen to be the mean radius R, i.e. $r_\pi = R_\pi = R$. We do this only after choosing a particular coordinate frame *xy* to work in as considerable simplifications take place.

3.4. Description in $\omega_0 = 0$ coordinate system

If we set in Eq. (49), $\omega_0 = 0$, i.e. orient our *xy* coordinate system so that the $\mathbf{r}_0$ lies along the positive *x*-axis (see Fig. 4 (center)), we obtain:

$$\frac{r_0}{r_\omega} = \frac{a(1-\cos\omega)}{(2a - r_0)\cos^2\alpha} + \cos\omega - \tan\alpha\sin\omega \qquad (50)$$

where we have also used Eq. (47) with $\omega_0 = 0$.

The vector $\mathbf{r}$ can be obtained by the following ansatz:

$$\mathbf{r} = x(\omega)\frac{\mathbf{r}_0}{r_0} + y(\omega)\frac{(\mathbf{L}\times\mathbf{r}_0)}{Lr_0} \qquad (51)$$

with

$$x(\omega) = r_\omega\cos\omega \qquad (52)$$

$$y(\omega) = r_\omega\sin\omega \qquad (53)$$

The velocity vector $v = \dot{\mathbf{r}}$ can be obtained by direct differentiation of Eq. (51).

It is instructive to study the polar plot of r_ω shown in Fig. 5 for different values of $\pm\alpha$ and the same initial kinetic energy. It is seen that for $\alpha > 0$ ($\alpha < 0$) the orbit is longer (shorter) as r_ω has to increase (decrease) due to condition Eq. (30) evaluated at entry. Thus, the two orbits corresponding to positive and negative values of α have to lie on identical ellipses (same semi major axis *a* and semi minor axis *b*), but with different orientations in the *xy* coordinate system. The dependence of the angle ω_ϵ of the eccentricity vector $\boldsymbol{\epsilon}$ on the entry angle α is also shown in Fig. 5 (lower right) obtained from conditions of Eqs. (44) and (45) evaluated for $\omega_0 = 0$. Eq. (50) is the well-known form introduced by Purcel [2] and discussed in more detail by Rudd [54], Hadjarab and Erskine [6] and Louette et al. [9]. For $\omega = \pi$, Eq. (50) is seen to be independent of the sign of α as required for first order focusing [2]. This is demonstrated graphically in Fig. 5.

We also compute α_ω using its definition Eq. (31) and Eqs. (39), (40), (44), (45) and (50):

$$\alpha_\omega = \arctan\left[\frac{\sin(2\alpha+\omega) - \frac{r_0}{a}\cos\alpha\sin(\alpha+\omega)}{1+\cos(2\alpha+\omega) - \frac{r_0}{a}\cos\alpha\cos(\alpha+\omega)}\right] \qquad (54)$$

We note that α_ω is an odd function of α at $\omega = 0$ and $\omega = \pi$. For a *circular* principal ray $a = r_0 = R_0$ and so $\alpha_\omega = 0$ for all values of ω. A typical plot of α_ω is given in Fig. 6 for $\tau = 1$ and $\alpha = 0, \pm 2°$ for the paracentric case of $R_0 = 82.55$, $R_\pi = R$, $\gamma = 1.5$ ($a = 92.075$) and for central entry with $R_0 = R_\pi = R = 101.6$, $\gamma = 1$ ($a = 101.6$).

The time-of-flight Δt_π for deflection through $\Delta\omega = \pi$, can be readily computed in analytic form using:

$$\Delta t_\pi = \int_0^\pi \frac{m r_\omega^2}{L}\,\mathrm{d}\omega = \sqrt{\frac{m r_0^6\left(\frac{2a}{r_0}-1\right)^3}{qka^3}}\cos^3\alpha \times \int_0^\pi \frac{\mathrm{d}\omega}{\left[1 - \frac{r_0}{a}\cos\alpha\cos(\alpha+\omega) + \cos(2\alpha+\omega)\right]^2} \qquad (55)$$

However, its expression is cumbersome in this coordinate system. A simpler expression is given in the next section in the $\omega_\epsilon = 0$ coordinate frame. A more useful expansion in powers of α is given (valid to better than 0.01% for the parameters of interest here), which also shows that only odd powers survive:

$$\Delta t_\pi = \sqrt{\frac{ma^3}{qk}}\left\{\pi + \sqrt{\left(\frac{2a}{r_0}-1\right)}\left[4\alpha + -2\left(\frac{8a}{3r_0}-1\right)\alpha^3 + \frac{1}{30}\left(\frac{1}{2a-r_0} + \frac{144a}{r_0^2} - \frac{32}{r_0}\right)\alpha^5 + \mathrm{O}[\alpha^7]\right]\right\} \qquad (56)$$

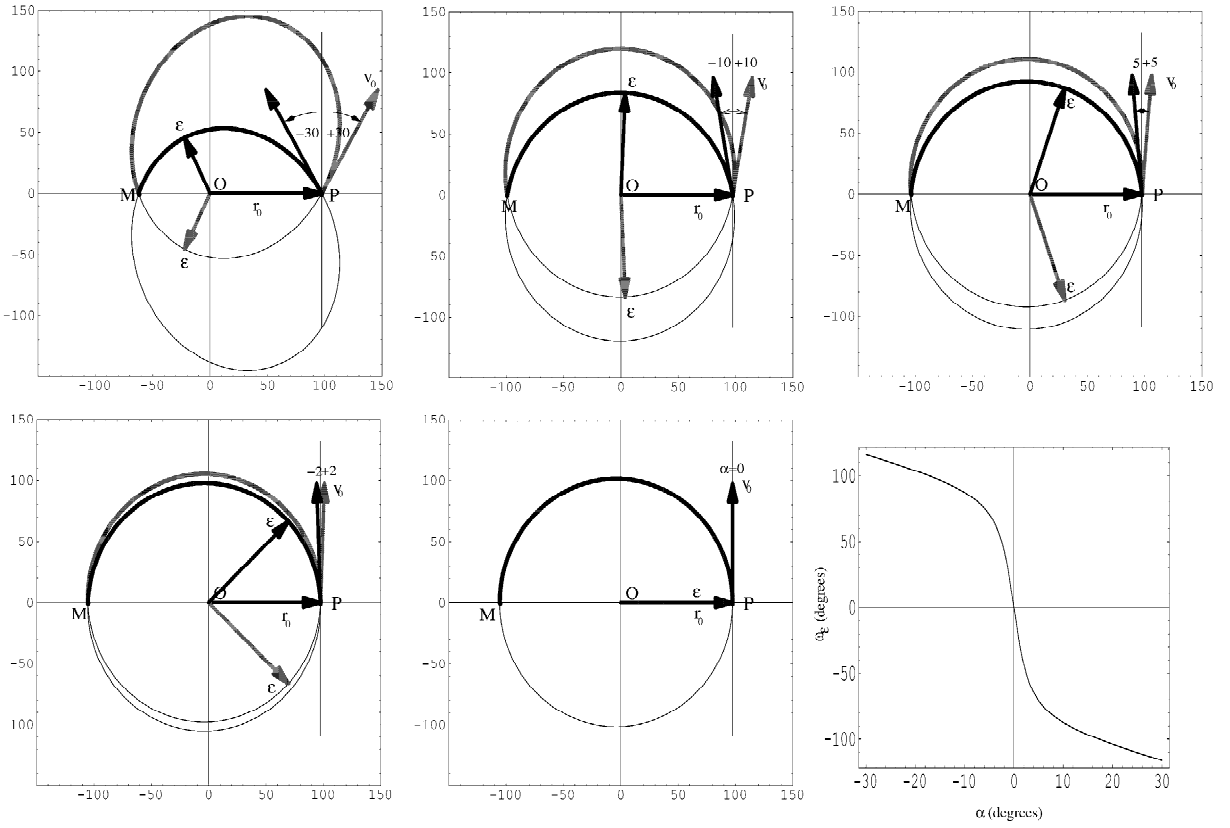

Fig. 5. Motion in the $\omega_0 = 0$ frame for various values of $\pm\alpha$. From left to right: $\alpha = \pm 30$, ± 10, ± 5, ± 2 and $0°$. The kinetic energy in all cases was the same and equal to the tuning energy, i.e. $t = w = 1000$ eV. Here we use the HDA parameters of Table 1 and $r_0 = 97.6$ mm. POM is the nodal line also shown in Fig. 3. The actual orbits from ω_0 to $\omega_0 + \pi$ are shown in bold. All outer orbits (in upper half-plane) have $\alpha > 0$ with the corresponding $\boldsymbol{\epsilon}$ lying in the lower half plane. As α decreases the corresponding eccentricity vectors rapidly rotate towards the positive x-axis. For $\alpha = 0$ they overlap. Note that the magnitude of $\boldsymbol{\epsilon}$ has been scaled to have length $r_{\min}$ for better viewing. The lower right figure shows the dependence of the angle ω_ϵ of the vector $\boldsymbol{\epsilon}$ on the entry angle α.

Eq. (56) shows that the time-of-flight for $\alpha < 0$ will always be shorter than for orbits with $\alpha > 0$. This is consistent with Kepler's first law and Fig. 5 where it is clear that the areas swept out for $\alpha < 0$ are always smaller than the corresponding areas for $\alpha > 0$.

We finally note that from the form of Eq. (50) one can readily derive as a special case the more traditional form (see for example Refs. [9,54]):

$$\frac{r_0}{r_\omega} = \frac{R_0 K_\alpha}{r_0 K_0} \frac{(1 - \cos\omega)}{\cos^2\alpha} + \cos\omega - \tan\alpha \sin\omega \quad (57)$$

where K_0 is the entry kinetic energy $K_0 = \frac{1}{2}mv^2 = t + q\tilde{V}(r_0)$, while $K_\odot$ is the kinetic energy of the reference principal ($\alpha = 0$) ray that describes a *circular* orbit with radius R_0 and for which it can easily be shown that $qk = 2R_0K_\odot$. Thus, Eq. (50) is seen to be the generalization of Eq. (57) for the case of an *elliptical* principal ray with different entry and exit radii (i.e. $R_0 \neq R_\pi$).

3.5. Description in $\omega_\epsilon = 0$ coordinate system

If we set in Eq. (49), $\omega_\epsilon = 0$, i.e. orient our coordinate system so that $\boldsymbol{\epsilon}$ lies along the positive x-axis, (see Fig. 4 (right)), we obtain:

$$\frac{r_0}{r_\omega} = \frac{r_0}{p} + \frac{\tan\alpha}{\sin\omega_0}\cos\omega = \frac{r_0}{p}(1 + \epsilon\cos\omega) \quad (58)$$

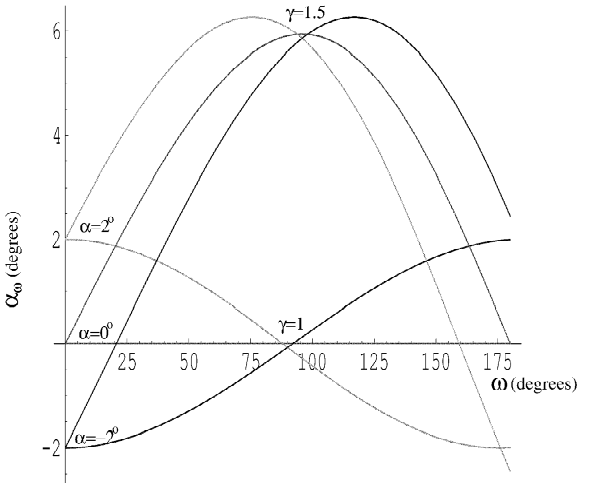

Fig. 6. Plot of α_ω (see Eq. (54)) for $\tau = 1$ and $\alpha = 0, \pm 2°$ for the paracentric case of $R_0 = 82.55$ mm, $R_\pi = R = 101.6$ mm, $\gamma = 1.5$ ($a = 92.075$ mm) and for central entry with $R_0 = R_\pi = R = 101.6$ mm, $\gamma = 1$ ($a = 101.6$ mm).

$$= \frac{a(1-\cos\omega)}{(2a - r_0)\cos^2\alpha} \times \left[1 + \sqrt{\sin^2\alpha + \left(1 - \frac{r_0}{a}\right)^2 \cos^2\alpha}\right] \cos\omega \tag{59}$$

This form is not very useful for obtaining focusing characteristics that depend on α since the entry point occurs at angle ω_0 obtained by setting $\omega_\epsilon = 0$ in Eqs. (44) and (45). However, the orientation of the orbit in the coordinate system for $\omega_\epsilon = 0$ leads to a vector form of the orbit useful in tracking the particle in three dimensions and obtaining its time of flight.

The vector $\mathbf{r}$ can be obtained by the following ansatz [47,75]

$$\mathbf{r}(t) = x(t)\frac{\boldsymbol{\epsilon}}{\epsilon} + y(t)\frac{\mathbf{L}\times\boldsymbol{\epsilon}}{L\epsilon} \tag{60}$$

where $r = 0$ is at the focus of the ellipse (point O in Fig. 7) and

$$x(t) = a(\cos\zeta - \epsilon) \tag{61}$$

$$y(t) = a\sqrt{(1-\epsilon^2)}\sin\zeta \tag{62}$$

$$t = \sqrt{\frac{ma^3}{qk}}(\zeta - \epsilon\sin\zeta) \tag{63}$$

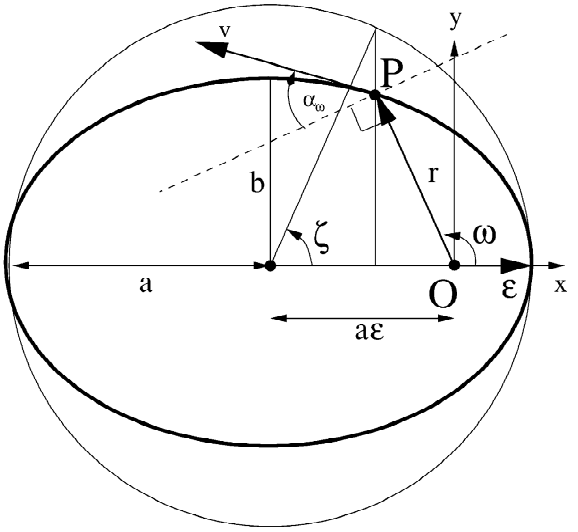

Fig. 7. Elliptical particle orbit in the *xy* (for $\omega_\epsilon = 0$) coordinate system showing the *true anomaly* ω and the *eccentric anomaly* ζ. O is the center of attraction and focus of the ellipse. The eccentricity vector $\boldsymbol{\epsilon}$ is seen to start from O and point to periapse. It thus *always lies along the semi major axis a* of the ellipse. Its length has been renormalized to $r_{\min}$ for better viewing. The general velocity angle α_ω is also shown.

with the particle being at periapse for time $t = 0$ and $\zeta = \omega = 0$ [47].

Eq. (60) may be directly differentiated with respect to time to obtain the vector $v = \dot{\mathbf{r}}$ (remembering that $\boldsymbol{\epsilon}$ and $\mathbf{L}$ are constants of the motion).

The new angle ζ introduced above is known as the Kepler [75] or eccentric [49] anomaly and is related to the angle ω (also known as the true anomaly) [49]:

$$\cos\zeta = \frac{\epsilon + \cos\omega}{1 + \epsilon\cos\omega} \tag{64}$$

as can easily be derived with the help of Fig. 7. A very useful conversion formula between the two anomalies that also avoids quadrant ambiguity ($\zeta/2$ is always in the same quadrant as $\omega/2$) is [49]:

$$\tan\frac{\zeta}{2} = \sqrt{\frac{1-\epsilon}{1+\epsilon}}\tan\frac{\omega}{2} \tag{65}$$

We may also use Eq. (64) to directly express the radius in terms of the eccentric anomaly [49]:

$$r = a(1 - \epsilon\cos\zeta) \tag{66}$$

Eq. (63) is also very useful since it gives directly the time-of-flight as a function of the eccentric anomaly ζ. Thus, for a particle entering at $t = t_0$ with ω_0, $\mathbf{r}_0$ and v_0 and exiting at an angle $\omega_0 + \delta$ later, we have using Eqs. (44) and (45) with $\omega_\epsilon = 0$ to define ω_0 and Eq. (65):

$$\begin{aligned}\Delta t(\omega_0, \delta) t\zeta(\omega_0 + \delta)) - t(\zeta_0) \\ = \sqrt{\frac{ma^3}{qk}} \{[\zeta(\omega_0 + \delta) - \epsilon \sin \zeta(\omega_0 + \delta)] \\ - (\zeta_0 - \epsilon \sin \zeta_0)\}\end{aligned} \tag{67}$$

which for deflection by $\delta = \pi$ then gives the time of flight Δt_π also computed in the $\omega_0 = 0$ coordinate system above:

$$\begin{aligned}\Delta t_\pi &\equiv \Delta t(\omega_0, \delta = \pi) \\ &= \sqrt{\frac{ma^3}{qk}} [\zeta_\pi - \zeta_0 - \epsilon(\sin \zeta_\pi - \sin \zeta_0)]\end{aligned} \tag{68}$$

with $\zeta_0 \equiv \zeta(\omega_0)$ and $\zeta_\pi \equiv \zeta(\omega_0 + \pi)$.

Using either Eq. (51) or Eq. (60), it is straightforward to describe the 3-D trajectory in any fixed coordinate system XYZ in which the initial components of $\mathbf{L}$ and $\boldsymbol{\epsilon}$ are known. These are directly computed from the initial position and velocity vectors $\mathbf{r}_0$ and v_0 whose components in the XYZ system can be readily obtained (see Appendix C). In Fig. 3 we show such a 3-D plot made with the help of the software program *Mathematica* using the vector form of Eq. (60).

4. Boundary conditions

In this analysis the region outside the analyser (region I) (see Fig. 9) will be at constant potential (free motion), while the region inside the analyser (region II) will be governed by the potential given by Eq. (2). Thus, the potential is seen to have a sharp step going across the boundary of the two regions.

This can be represented mathematically by a potential with step at $\theta = \pi/2$:

$$V(r, \theta) = V(r) u\left(\frac{\pi}{2} - \theta\right) + V_p u\left(\theta - \frac{\pi}{2}\right) \tag{69}$$

with $V(r)$ given by Eq. (2) and $u(x)$ is the *Heaviside* unit step function. Then, $u(\pi/2 - \theta)$ is given by:

$$u\left(\frac{\pi}{2} - \theta\right) = \begin{cases} 0 & \text{for } \dfrac{\pi}{2} < \theta < \pi \quad \text{Region I} \\ 1 & \text{for } 0 \le \theta \le \dfrac{\pi}{2} \quad \text{Region II} \end{cases} \tag{70}$$

while $u(\theta - \pi/2)$ has the ranges of values 1 and 0 reversed.

In Appendix B, we prove mathematically that in crossing this discontinuity, the potential energy is indeed conserved (even though there is an infinite force at the boundary due to the step) and the particle is refracted at the potential boundary $\theta = \pi/2$ both at the entry and the exit of the HDA.

Refraction is usually ignored in most treatments having to do with narrow slit spectrometers since in this case it is practically negligible (see below). In cases, however, where narrow slits are not used, as for example in the early work on HDAs [2], in the description of two-stage tandem HDA spectrometers [66] or spectrographs [25] and in treatments of modern HDAs utilizing PSDs (see for example Refs. [6,62]), refractive effects in crossing from region I to region II are usually important and have been treated analytically within a step-potential model (as above). Wollnik and collaborators [14,16] however, have used more elaborate (albeit tedious) analytic and numerical treatments by modeling the HDA fringing fields in various approximations (for more details see also the review [61] and book [22] by Wollnik). Now-a-days, accurate trajectory calculations can be readily performed on a PC using specialized ion-optics programs such as SIMION [12]. We use this approach in papers II and III, when more accurate modeling of the fringing fields is required. It is interesting to note, however, that even though the solution of the potential distribution of the fringing fields for both a shielded (the $\theta = \pi/2$ potential boundary is grounded) HDA [42] and an open (no potential boundary assumed) spherical sector [41] are known analytically, all studies to date have preferred to actually solve Laplace's equation numerically (see for example Ref. [17]) for the potential and then use this numerical solution to investigate the effects of the fringing fields.

4.1. Energy conservation across potential boundary

In region I (outside the analyser), the particle has a kinetic energy t with

$$t = \frac{1}{2} m v^{*2} \tag{71}$$

Thus, its total energy E^* is equal to its kinetic energy t plus potential energy qV_p due to the decelerating potential V_p, while inside the analyser it has a total energy equal to the sum of its kinetic and potential energies, K and qV. We reserve the symbol * for marking quantities of region I that could otherwise be confused with corresponding quantities in region II. Applying the conservation of energy on either side of the HDA boundary (as proved in Appendix B.1) we obtain:

$$\begin{aligned} t + qV_p &= K(r) + qV(r) \\ &= \frac{1}{2} m v^2 + q\tilde{V}(r) + qV_p \end{aligned} \tag{72}$$

$$E^* = E + qc + qV_p \tag{73}$$

and thus,

$$E = t - qc = E^* - qc - qV_p \tag{74}$$

where E is the *effective* total energy inside the analyser found to be conserved in Eq. (20) and is negative for bound motion. It is seen from Eq. (74) that the two total energies E^* and E just differ by a constant. Energy E^* is referred to zero potential, while E is referred to the potential $q(c + V_p)$ as seen from the definition of the potential $V(r)$ in Eq. (2). Thus, the constant c is seen to be needed only to match the energies E and E^* inside and outside the HDA. It only comes into play when the outside energies t or E^* are used in the trajectory equations. Furthermore, we note that from Eq. (72) we obtain the useful relation:

$$\frac{1}{2} m v^2 = t - q\tilde{V}(r) = t - (1 - \gamma)w \geq 0 \tag{75}$$

which necessarily puts a lower bound on the value of γ for a particle to go through the HDA, i.e. $t - (1 - \gamma)w \geq 0$ or $\gamma \geq 1 - \tau$.

Using Eq. (74) in the definition of the semi-major axis a we also have the useful relation:

$$a = \frac{qk}{2(qc - t)} \tag{76}$$

4.2. Particle refraction across potential boundary

In region I the potential is constant and the particle thus feels zero force, its velocity remains constant and therefore so does its angular momentum $L^* = mr_0 v_0^* \cos \alpha^*$. In region II, the force is central and therefore the angular momentum $L = mr_0 v_0 \cos \alpha$ is also conserved. However, because of the finite step potential at the boundary the two angular momenta are in general *not* equal.

Using Eq. (74) of energy conservation across the boundary we may relate v and v^*. It is shown in Appendix B.2 that we obtain the following relation between the angular momenta:

$$L^2 = L^{*2} \left[1 - \frac{q\tilde{V}(r_0)}{t \cos^2 \alpha^*} \right] \tag{77}$$

which expresses L in terms of the entry angle α^* (instead of α) and the potential $\tilde{V}(r_0)$. This relation may also be expressed as:

$$L \tan \alpha = L^* \tan \alpha^* \tag{78}$$

It then readily follows (see Appendix B.2) that:

$$v \sin \alpha = v^* \sin \alpha^* \tag{79}$$

or

$$v_r = v_r^* \tag{80}$$

and

$$v_\omega^2 - v_\omega^{*2} = -\frac{2q\tilde{V}(r_0)}{m} \tag{81}$$

From Eq. (80) it is seen that the radial velocity, $v_r = \dot{r}$, is continuous across the boundary [6], as opposed to the angular velocity, $v_\omega = r\dot{\omega} = L/mr$ which is not. This has the consequence that since only the magnitude of L is discontinuous and not also its direction, the particle remains on the same plane as it crosses the potential boundary. Thus, the angle β, which defines the plane of the orbit will not suffer any changes as the particle crosses the boundary. Eq. (79) is seen to be the charged-particle analog of Snell's law of refraction in optics [76].

4.3. Trajectory equations including refraction

Using Eqs. (77) and (78) we can include the refraction effects into the trajectory equation for the $\omega_0 = 0$ form (Eq. (50)) to obtain:

$$\frac{r_0}{r_\omega} = \frac{\left[1 - \frac{q\tilde{V}(r_0)}{t}\right]}{\left[1 - \frac{q\tilde{V}(r_0)}{t\cos^2\alpha^*}\right]} \frac{a(1-\cos\omega)}{(2a - r_0)\cos^2\alpha^*} + \cos\omega - \tan\alpha^*\left(\frac{L^*}{L}\right)\sin\omega \quad (82)$$

$$= \frac{qk(1-\cos\omega)}{2r_0 t\cos^2\alpha^*\left[1 - \frac{q\tilde{V}(r_0)}{t\cos^2\alpha^*}\right]} + \cos\omega - \frac{\tan\alpha^*\sin\omega}{\sqrt{1 - \frac{q\tilde{V}(r_0)}{t\cos^2\alpha^*}}} \quad (83)$$

We may now specify the values of constants k and c (via $\tilde{V}(r_0)$) appearing in Eq. (83). This is usually done by specifying a principal reference ray with $\alpha = 0$ and *nominal* pass energy t set to the tuning energy w, i.e. $t = w$. Here, we define our principal ray such that it enters at $r = R_0$ (i.e. $r_0 = R_0$) and exits after a deflection by 180° at $r = R_\pi$ (i.e. $r_\pi = R_\pi$). Thus, using the trajectory equation Eq. (50) with $r_0 = R_0$, $r = R_\pi$, $\alpha = \pi$, $t = w$ and the potential equation (Eq. (2)) at $r = R_0$ we have:

$$\frac{R_0}{R_\pi} = \frac{qk}{R_0(w - qc) + qk} - 1 \quad (84)$$

$$q\tilde{V}_0 = -\frac{qk}{R_0} + qc \quad (85)$$

Using the definition of γ from Eq. (3), we may now solve Eqs. (84) and (85) simultaneously for k and c yielding:

$$qk = \gamma w R_0\left(1 + \frac{R_0}{R_\pi}\right) = wR_0(1+\xi)\frac{\gamma}{\xi} \quad (86)$$

$$qc = w\left(1 + \gamma\frac{R_0}{R_\pi}\right) = w\left(1 + \frac{\gamma}{\xi}\right) \quad (87)$$

we may also replace qc and qk above in Eq. (41) and obtain a new equation for the semimajor axis a as:

$$a = \frac{R_0(1+\xi)\frac{\gamma}{\xi}}{2\left(1 + \frac{\gamma}{\xi} - \tau\right)} \quad (88)$$

We now replace both qk and qc (or equivalently a from Eq. (88)) in Eqs. (50) and (83) to obtain the final trajectory equation in terms of the entry angle α and/or α^*.

From Eq. (50) we have:

$$\frac{r_0}{r_\omega} = \frac{qk(1-\cos\omega)}{2[qk - r_0(qc - t)]\cos^2\alpha} + \cos\omega - \tan\alpha\sin\omega \quad (89)$$

$$= \frac{1-\cos\omega)}{2\left[1 - \frac{r_0}{R_0}\frac{\xi\left(1 + \frac{\gamma}{\xi} - \tau\right)}{\gamma(1+\xi)}\right]\cos^2\alpha} + \cos\omega - \tan\alpha\sin\omega \quad (90)$$

From Eq. (83) we have:

$$\frac{r_0}{r_\omega} = \frac{1}{2}\frac{\gamma}{\tau}\frac{R_0}{r_0}\frac{\left(1 + \frac{1}{\xi}\right)}{\left[1 - \frac{\frac{q\tilde{V}(r_0)}{w}}{\tau\cos^2\alpha^*}\right]}\frac{(1-\cos\omega)}{\cos^2\alpha^*} + \cos\omega - \frac{\tan\alpha^*}{\sqrt{1 - \frac{\frac{q\tilde{V}(r_0)}{w}}{\tau\cos^2\alpha^*}}}\sin\omega \quad (91)$$

and after expanding $q\tilde{V}(r_0)$ using Eqs. (86) and (87):

$$q\tilde{V}(r_0) = -\frac{qk}{r_0} + qc = w\left\{1 + \gamma\left[\frac{1}{\xi} - \left(\frac{1}{\xi} + 1\right)\frac{R_0}{r_0}\right]\right\} \quad (92)$$

we obtain:

$$\frac{r_0}{r_\omega}=\frac{1}{2}\frac{\gamma}{\tau}\frac{R_0}{r_0}\times\frac{\left(1+\frac{1}{\xi}\right)}{\left[1-\frac{1+\gamma\left[\frac{1}{\xi}-\frac{R_0}{r_0}\left(1+\frac{1}{\xi}\right)\right]}{\tau\cos^2\alpha^*}\right]}\times\frac{(1-\cos\omega)}{\cos^2\alpha^*}+\cos\omega-\frac{\tan\alpha^*}{\sqrt{1-\frac{1+\gamma\left[\frac{1}{\xi}-\frac{R_0}{r_0}\left(1+\frac{1}{\xi}\right)\right]}{\tau\cos^2\alpha^*}}}\times\sin\omega \tag{93}$$

We may now also use the value of qk to evaluate E and p to determine the type of conic section the particle follows. For the principal trajectory ($t=w$, $r_0=R_0$ and $\alpha=0$) we define the *principal* ray parameters: energy, latus rectum $\bar{p}$, semi major axis and time-of-flight Δt_π. Directly from Eqs. (74), (39), (88) and (56) we have:

$$\bar{E}\equiv w-qc=-w\frac{\gamma}{\xi} \tag{94}$$

$$\bar{p}\equiv\frac{2R_0^2w}{qk}=\frac{2R_\pi}{\gamma(1+\xi)} \tag{95}$$

$$\bar{a}\equiv\frac{1}{2}R_0(1+\xi)=\frac{1}{2}(R_0+R_\pi) \tag{96}$$

$$\bar{\Delta t}_\pi\equiv\pi\sqrt{\frac{m\bar{a}^3}{qk}}=\frac{\pi}{2}R_0(1+\xi)\sqrt{\frac{m\xi}{2w\gamma}} \tag{97}$$

Thus, for $\gamma>0$ we always have $\bar{E}<0$ leading to elliptical orbits. For elliptical orbits, the quantity $\frac{1}{2}|r_{\max}+r_{\min}|=|r(\omega=\omega_\epsilon+\pi)+r(\omega=\omega_\epsilon)|$ is the semi-major axis a, which is always aligned along the eccentricity vector $\boldsymbol{\epsilon}$ and is given by Eq. (41), while the semi minor axis b is given by $b=a\sqrt{1-\epsilon^2}$. As already seen, a only depends on the effective total energy E and is independent of the entry angle, while b does also depend on the entry angle α via the eccentricity ϵ (see Eq. (19)). Thus, in the case of the elliptical orbit Eq. (17) reduces to the well known elliptical form:

$$r_\omega=\frac{a(1-\epsilon^2)}{1+\epsilon\cos(\omega-\omega_\epsilon)} \tag{98}$$

with a and ϵ given by Eqs. (41) and (19), respectively.

4.4. Spectrograph basic equation

Since the HDA focusing properties can be studied only from the ray trace on the exit plane, an expression which gives the position of the particle at the image (exit), as a function of its position and direction at the object (entrance) and its *nominal* (reduced) pass energy τ is needed. Directly from Eq. (50) and using Eq. (76) we have:

$$r_\pi=\frac{r_0[qk+r_0(t-qc)]}{qk\tan^2\alpha-r_0(t-qc)} \tag{99}$$

$$=\frac{r_0}{1+\cos^2\alpha\left\{\frac{r_0}{R_0}\frac{\left[1+\frac{\xi}{\gamma}(1-\tau)\right]}{(1+\xi)}-1\right\}} \tag{100}$$

which is the form of r_π expressed as a function of α. If we now include the refraction and substitute for $\tan\alpha$ using Eq. (B.24) in Eq. (83) we get the surprisingly simple result:

$$r_\pi=-r_0+\frac{qk}{qc-t\cos^2\alpha^*} \tag{101}$$

$$=-r_0+\frac{R_0(1+\xi)}{1+\frac{\xi}{\gamma}(1-\tau\cos^2\alpha^*)} \tag{102}$$

Eq. (101) is seen to be a much simpler expression than Eq. (99). In fact, to our knowledge, this form of the equation is new and has never appeared in the literature to date. It expresses very simply the exit point r_π after deflection by 180° in terms of the kinetic energy t ($=T-qV_p$ in the case of preretardation when $V_p\neq 0$—see Eq. (1)), entry angle α^* (prior to refraction) and entry radius r_0 for known potential $\tilde{V}(r)=-k/r+c$.

The relation between r_π and r_0 (Eqs. (99)–(102)) is known [77] as the *basic equation* of the spectrograph. From this all further properties of the HDA may be extracted (see paper II). Eq. (101) expresses the relation between r_π and r_0 in a very simple form in terms of the potential $\tilde{V}(r)$ parameters *qk* and *qc* and is conveniently independent of the particular HDA parameters such as R_1, R_2, R_0, V_0, V_1, V_2. Eq. (102) on the other hand is conveniently written in terms of the spectrometer parameters. Both forms will be used. For the case of a conventional HDA we have $\gamma = \xi = 1$ and the basic equation in this case may be rearranged into the usual form:

$$\frac{(r_\pi - R_0)}{R_0} = -\frac{(r_0 - R_0)}{R_0} - 2\left[1 - \frac{1}{1 + \sin^2\alpha^* - (\tau - 1)(1 - \sin^2\alpha^*)}\right] \quad (103)$$

Eq. (103) is seen to be identical[2] with Eq. (8) of Hadjarab and Erskine [6]. The results of Ref. [6] also include the refraction correction at the entrance of the HDA.

In Eqs. (101) and (102), the sum $r_{0,\pi} \equiv r_\pi + r_0$ is the *range* of the trajectory. It is seen to have a few interesting properties: Eq. (101) shows that for fixed *qk* and *qc* (i.e. fixed voltages V_1 and V_2 on the HDA) the range $r_{0,\pi}$ is *independent of the entry or exit positions* (for the same energy t and angle α^*). This is hidden in Eq. (99) since α is not anymore and independent variable but a function of the entry variables α^* and r_0. In other words, the distance traveled in the plane of the orbit is always the same (for the same energy t and angle α^*) no matter where the entry or exit is made. Clearly, this is not so in Fig. 1, where it is seen that the central entry has a much longer range than the paracentric entry. This must be a manifestation of the fringing fields. In this light, it is also rather surprising that the exit points r_π for both central and paracentric entries in Fig. 1 is roughly the same. We shall discuss these points in more detail in paper III. Here, our main goal was to obtain Eqs. (101) or (102).

Eq. (102) also shows that the range $r_{0,\pi}$ is a universal function of the 'reduced' pass-energy τ and the incident angle α^*. This, universal scaling with τ is particularly useful during the energy calibration of the spectrometer since different energies T and deceleration factors F must all fall on one universal curve dependent on τ, avoiding the tedious task of calibrating the spectrometer for all combinations of F, T and W utilized in a measurement. The energy calibration is discussed in more detail in paper II.

In Table 2 we present typical numerical values of the trajectory parameters. A comparison between central and paracentric parameters is made. In both cases the parameters of the principal ray are given. An example is also given where the energy of the particle is slightly larger than the tuning energy. For generality, for these cases the particle is made to enter at an angle $\phi_0 \neq 0$. This then defines the angle Φ_0 given ($\Phi_0 = \phi_0 - \pi$; see Fig. 3). The large value of $\alpha^* = \pm 30°$ is used on purpose even though rather exaggerated as it allows for bigger differences in the numbers. The table gives a feeling for the magnitude of the parameters involved and can also be used to check formulas.

We also plot the effective potentials U_{eff} that corresponds to the parameters of Table 2 defined as:

$$U_{\text{eff}}(r) \equiv q\tilde{V}(r) + \frac{L^2}{2mr^2} \quad (104)$$

in which the particles are moving as a function of r (see Fig. 8 top) and angle ω (see Fig. 8 bottom) as ω varies along the orbit from ω_0 to $\omega_0 + \pi$. The paracentric potential is seen to always be deeper (E is more negative) and for the example shown the particle trajectories with $\alpha = \pm 30°$ are much closer to the $\alpha^* = 0$ trajectory than in the case of the central entry potential.

4.5. Analyser voltages

The voltage scheme V_1 and V_2 applied on the inner and outer spherical shells of the analyser, respectively, is a function of the tuning energy of the spectrograph. The determination of the voltages is based

[2] To see this we need to make the correspondence with the symbols used in Ref. [6], i.e. $\zeta_\pi \Leftrightarrow (r_\pi - R_0)/R_0$, $\zeta_0 \Leftrightarrow (r_0 - R_0)/R_0$ and $\Delta E/E \Leftrightarrow (t - w)/w = \tau - 1$.

Table 2
Comparison of paracentric and conventional entry orbital parameters computed for electron ($q = -e$) passage through an *ideal* hemispherical deflector analyser (HDA) of the form $V(r) = -k/r + c$, with no preretardation (i.e. $F = 1$, $W = w$, $V_p = 0$) and planar (unrefracted) launching angle $\alpha^* = 0°$ and $\pm 30°$[a].

Parameters			Reference	Paracentric HDA				Conventional HDA			
	H	R_0 (mm)	Fig. 2	82.55	82.55	82.55	82.55	101.6	101.6	101.6	101.6
i	D	γ	Eq. (3)	1.5	1.5	1.5	1.5	1	1	1	1
n	A	T (eV)	Eq. (1)	1000	1020	1020	1020	1000	1020	1020	1020
p		W (eV)	Eq. (4)	1000	1000	1000	1000	1000	1000	1000	1000
u	en	r_0 (mm)	Fig. 2	82.55	79.184	79.184	79.184	101.6	98.3877	98.3877	98.3877
t	try	Φ_0 (°)	Fig. 3	0	−7.25515	−7.25515	−7.25515	0	−7.25515	−7.25515	−7.25515
		α^* (°)	Fig. 2	0	0	−30	30	0	0	−30	30
p											
o											
t		V_0 (V)	Eq. (3)	500	500	500	500	0	0	0	0
e		V_1 (V)	Eq. (109)	881.151	881.151	881.151	881.151	806.63	806.63	806.63	806.63
n		V_2 (V)	Eq. (109)	−502.903	−502.903	−502.903	−502.903	−446.483	−446.483	−446.483	−446.483
t		qk (eV-mm)	Eq. (86)	224 433	224 433	224 433	224 433	203 200	203 200	203 200	203 200
i		qc (eV)	Eq. (87)	2218.75	2218.75	2218.75	2218.75	2000	2000	2000	2000
a		f	Eq. (110)	1.38405	1.38405	1.38405	1.38405	1.25311	1.25311	1.25311	1.25311
l											
		α (°)	Eq. (B.22)	0	0	−23.2568	23.2568	0	0	−28.9945	28.9945
		E^* (eV)	Eq. (72)	1000	1020	1020	1020	1000	1020	1020	1020
		E (eV)	Eq. (20)	−1218.75	−1198.75	−1198.75	−1198.75	−1000	−980	−980	−980
t		v_0^* (mm/ns)	Eq. (71)	18.7553	18.9419	18.9419	18.9419	18.7553	18.9419	18.9419	18.9419
r		v_0 (mm/ns)	Eq. (75)	22.9704	23.9860	23.9860	23.9860	18.7553	19.5388	19.5388	19.5388
a		L^* (eV-ns)	Eq. (B.15)	8802.86	8527.94	7385.41	7385.41	10 834.3	10 596.1	9176.53	9176.53
j		L (eV-ns)	Eq. (B.16)	10 781.3	10 798.9	9921.41	9921.41	10 834.3	10 930.1	9560.15	9560.15
e		p (mm)	Eq. (39)	91.0897	91.3877	77.1395	77.1395	101.6	103.404	79.1083	79.1083
c		ϵ	Eq. (19)	0.103448	0.154118	0.419474	0.419474	0	0.0509845	0.486772	0.486772
t		a (mm)	Eq. (41)	92.0750	93.6112	93.6112	93.6112	101.6	103.673	103.673	103.673
o		b (mm)		91.5810	92.4928	84.9772	84.9772	101.6	103.539	90.5618	90.5618
r		r_π (mm)	Eq. (102)	101.600	108.038	75.198	75.198	101.6	108.959	66.1467	66.1467
y		r_{min} (mm)	Eq. (17)	82.55	79.184	54.3438	54.3438	101.6	98.3877	53.2081	53.2081
		r_{max} (mm)	Eq. (17)	101.6	108.038	132.879	132.879	101.6	108.959	154.139	154.139
		tof (ns)	Eq. (68)	13.9705	14.3215	6.91405	21.729	17.0185	17.5421	7.75394	27.3302
		tof (ns)	Eq. (56)	13.9705	14.3215	7.20557	21.4375	17.0185	17.5421	8.39616	26.688

[a] In the Ref. column appear the equation (or figure) numbers that refer to the equation (or figure) in the text used to compute (or define) the corresponding values. Some of the parameters refer to Fig. 3 and those given in Table 1. The mass of the electron $m = 5.68569$ eV-ns^2/mm^2, while in both cases $R_\pi = \underline{R} = 101.6$ mm. These results are independent of the launching angle β.

on the concept of *principal* ray, in a straightforward way. The entry and exit points are specified. For these points, the principal ray with $\alpha = 0$ (or $\alpha^* = 0$) and pass energy t, set to the analyser tuning energy w, i.e. $t = w$, is decided [55]. These conditions then define the proper potential applied on the analyser. In this study, the principal ray is defined such that a charged particle enters at $r = \underline{R}_0$ and exits after a deflection by $\Delta\omega = \pi$ at $r_\pi = \underline{R} \equiv (R_1 + R_2)/2$.

Applying voltages V_1 and V_2 on the inner and outer spherical shells of the analyser, respectively, the expressions for k and c are obtained:

$$c = \frac{R_2V_2 - R_1V_1}{\Delta R} - V_p \tag{105}$$

$$k = \frac{\Delta V}{\Delta R} R_1R_2 \tag{106}$$

Substituting k and c from the expressions above into the spectrograph basic equation Eq. (101), the principal ray case reduces to:

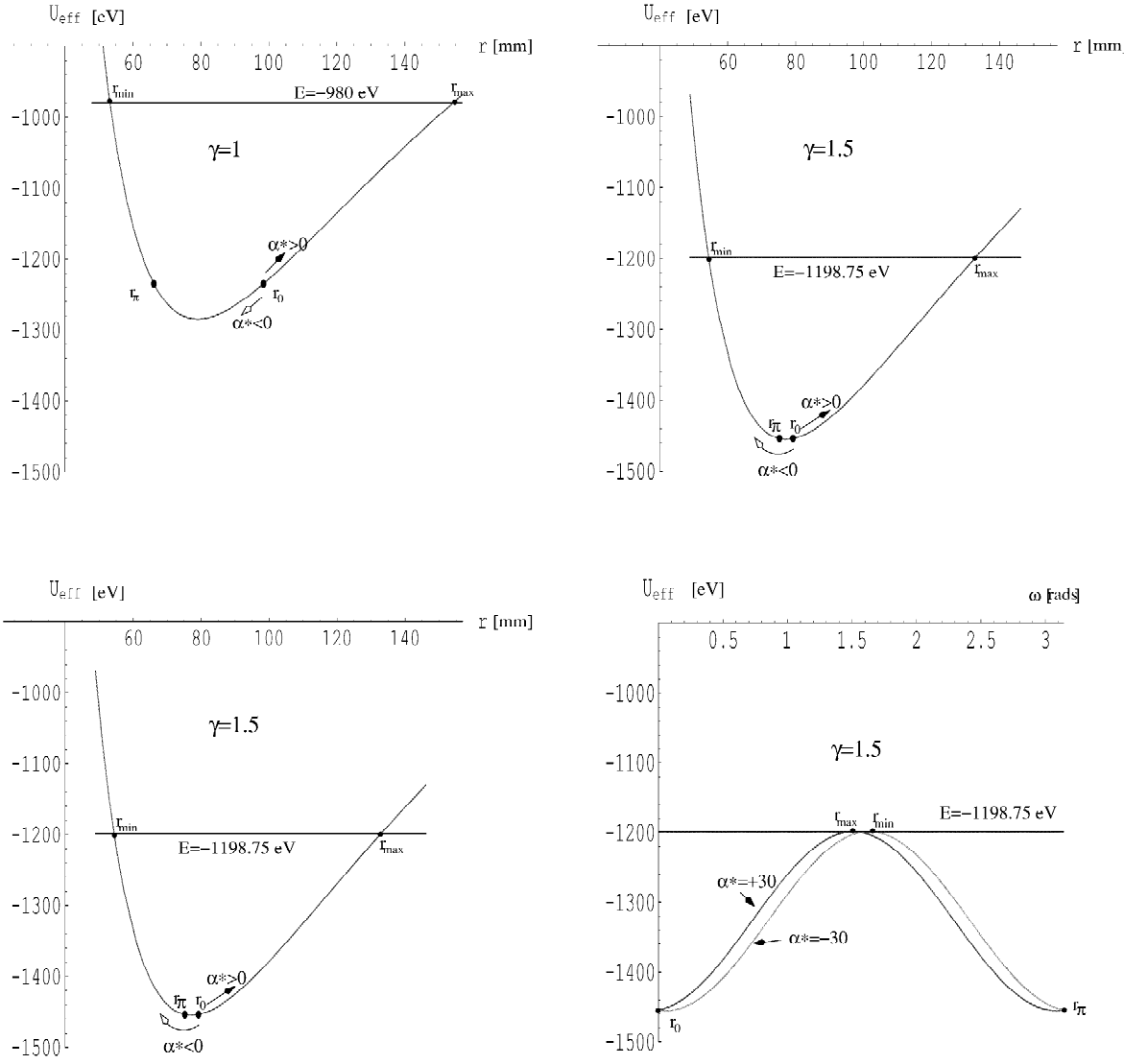

Fig. 8. Effective potential energy $U_{\rm eff}(r(\omega))$ plotted as a function of $r(\omega)$ (top) and as a function of ω (bottom) for the cases of $\alpha^* = \pm 30°$given in Table 2 with either $\gamma = 1$(left) or $\gamma = 1.5$ (right). The horizontal line is the total effective energy E in each case. $U_{\rm eff}(r)$ is the same for both angles $\alpha^* = \pm 30°$(top curves). The turning points $r_{\rm min}$ and $r_{\rm max}$ are shown. It is seen (darker lines in bottom figures) that for $\alpha^* > 0$ we also have $\partial r/\partial\omega > 0$, i.e. the particle follows an orbit in the direction of $r_{\rm max}$ according to Eq. (31), while for $\alpha^* < 0$ it follows a trajectory first going through $r_{\rm min}$. The arrows (top) point in the direction of motion from the starting point r_0.

$$R_\pi = -R_0 + \frac{q\,\Delta V\,R_1R_2}{q(V_2R_2 - V_1R_1) - w\,\Delta R} \tag{107}$$

where $\Delta R \equiv R_2 - R_1$ and $\Delta V \equiv V_2 - V_1$. Furthermore, for a pre-specified entrance potential V_0 (γ), after substitution of k and c, into Eq. (2), V_0 is written as:

$$V_0 = \frac{(R_2 - R_0)R_1V_1 + (R_0 - R_1)R_2V_2}{\Delta R\,R_0} \tag{108}$$

Solving Eqs. (107) and (108) for V_1 and V_2, and using the definitions Eqs. (3) and (7), the voltage equations are obtained:

$$qV_i = W - w\left(\frac{\gamma}{\xi}\right)\left[\frac{R_0(1+\xi)}{R_i} - 1\right] \quad i = 1, 2 \tag{109}$$

which uniquely determine V_1 and V_2 in terms of potentials V_0, V_p, the tuning energy w and the 'principal ray' positions of the entrance R_0 and the exit R_π, respectively. This is the most general formula for the voltages from which all specific cases may be derived. We note that the voltages V_i above are referenced to *ground*.

We also calculate the generalized spectrometer constant f:

$$f \equiv \frac{q\,\Delta V}{w} = \left(\frac{\gamma}{\xi}\right)\left(\frac{\Delta R}{R_1 R_2}\right)R_0(1+\xi) \tag{110}$$

The spectrometer constant has been introduced in the past for convenience, since it uniquely defines the appropriate potential difference across the analyser ΔV as a function of w (see for example Ref. [78]). In the more general paracentric HDA case, f is seen to be proportional to γ.

5. Summary and conclusions

We have presented a general treatment of charged particle motion in the *ideal* potential $\tilde{V}(r) = -k/r + c$ for more general launching conditions than what have been considered to date. Specifically, we obtained general trajectory equations in analytic form for r as a function of the deflection angle ω in which the reference principal ray describes an *elliptical* trajectory starting at R_0 at the arbitrary potential $V_0 = V(R_0)$ and exiting after deflection by π at R_π (see Eqs. (90) and (93)). Conventional trajectory equations are recovered as the special case $R_0 = R_\pi = R$ and $V_0 = V_p$, where V_p is the preretardation plate voltage of the analyser.

The finite potential at entry V_0 causes refraction to be non-negligible. A formal treatment of refraction at the potential boundary, assuming an idealized step function potential $V(r, \theta)$ to model the fringing fields, is given showing that the magnitude L of the particle's angular momentum suffers a finite change even though its direction remains unchanged, while its total energy is conserved. For $q(V_0 - V_p) < 0$ refraction always leads to smaller entry angles α. Useful analytical formulas are obtained for both the scalar and vector form of the orbits allowing for their convenient graphical representation in two and three dimensions. The time-of-flight (tof) of the particles is also obtained in closed analytical form and a Taylor series expansion around $\alpha = 0$explicitly shows that tofs with $\alpha < 0$ are always smaller than those with $\alpha > 0$, since the path is also correspondingly smaller. Clearly, when $q(V_0 - V_p) < 0$ the particles are accelerated at the potential boundary at entry leading to smaller tofs. The basic equation of the spectrograph is also obtained as a function of α and α^*, where α^* is the entry angle prior to refraction. The form written in terms of α^* is found to have a surprisingly simple expression in terms of the constants qk and qc (Eq. (101)). This form is much simpler than the one obtained in terms of α (Eq. (99)), arguing in favor of always including refraction corrections. In II we use the basic spectrometer equation derived here to investigate the operation and optical properties of the ideal HDA and see how they are altered by the effects of the fringing fields by comparing with ion-optics simulations using SIMION and experimental results obtained from laboratory measurements using our paracentric HDA.

Finally, we have also stressed some particular properties of Kepler orbits that relate to the launching angle α and which are not so well known: (a) The *eccentricity* vector $\boldsymbol{\epsilon}$ is *conserved* and always points to periapse, (b) particles with entry angle $\alpha < 0$ ($\alpha > 0$) will move towards (away from) periapse and will have correspondingly shorter (longer) time-of-flights for deflection through the same angle $\Delta\omega$, (c) the range $r_{0,\pi}$, for deflection through $\Delta\omega = 180°$, is *independent* of the entry and exit points r_0 and r_π for the same entry angle α^* and kinetic energy t. In III we shall investigate how these properties hold-up when strong fringing fields are present at the entrance and exit of an HDA with large interradial separation.

Acknowledgements

We would like to acknowledge meaningful discussions with J. Erskine, D. Roy, E. Sidky, H. Wollnik,

R. Woodard and M.I. Yavor. We also thank Pat Richard, director of the JRML for his constant support and interest throughout this work. This work has received partial support from the Greek Ministry of Research and Technology and the Chemical Sciences, Geosciences and Biosciences Division, Office of Basic Energy Sciences, Office of Science, US Department of Energy.

Appendix A. Reference table of symbols

An alphabetical list of the most important symbols used in this paper is given for convenience in Table A.1

Table A.1. List of symbols and short explanation

a	semi-major axis
b	semi-minor axis
c	$\tilde{V}(r) = -\frac{k}{r} + c$
d_i	diameter of HDA entry aperture
d_{PSD}	diameter of PSD
E	conserved total energy
f	spectrometer constant, $f = \frac{q\ \Delta V}{w}$
F	deceleration ratio, $F = \frac{W}{w}$
k	$\tilde{V}(r) = -\frac{k}{r} + c$
K	kinetic energy
L	angular momentum
m	mass of particle
p	*latus rectum*
q	particle charge ($q = -e$ for electron)
r	radius of orbit
$r_{\min}$	minimum radius
$r_{\max}$	maximum radius
r_0	radius at HDA entry
R_0	principal ray entry radius
R_π	principal ray exit radius
R_1	HDA inner radius
R_2	HDA outer radius
R	HDA mean radius
t	particle kinetic energy (before refraction), $t = K^*$
T	particle kinetic energy far from HDA
$u(x)$	unit step function at $x = 0$
v	particle velocity
v_r	radial component of particle velocity
v_ω	angular component of particle velocity
$V(r)$	HDA potential, $V(r) = \tilde{V}(r) + V_{\mathrm{p}}$
$\tilde{V}(r)$	$\tilde{V}(r) = -\frac{k}{r} + c$
V_0	nominal voltage $V(R_0)$
V_1	nominal voltage $V(R_1)$ on R_1
V_2	nominal voltage $V(R_2)$ on R_2
w	HDA tuning energy after deceleration
W	HDA tuning energy prior to deceleration
α	launching angle in plane of orbit (Figs. 2 and 3)
β	angle of orbital plane (Fig. 3)
γ	control parameter to set V_0, (Eq. (3))
$\delta(x)$	δ-function at $x = 0$
ϵ	eccentricity
$\boldsymbol{\epsilon}$	eccentricity vector
ζ	eccentric anomaly (angle)
θ	polar angle in $\{r, \theta, \phi\}$ system
τ	fractional pass energy, $\tau = \frac{t}{w}$
ϕ	azimuthal angle in $\{r, \theta, \phi\}$ system
ϕ_0	azimuthal angle at entry
ξ	HDA parameter $\xi = \frac{R_\pi}{R_0}$
ω	angular coordinate in orbital plane
ω_0	*omega* at entry of HDA
ω_ϵ	ω at periapse
$\dot{\omega}$	particle angular speed
$*$	designates quantities prior to HDA entry (before refraction)

Appendix B. Boundary conditions

B.1. Energy conservation across potential boundary

In the absence of a time-dependent magnetic field Maxwell's equations require that $\nabla \times \boldsymbol{\mathscr{E}} = 0$. Equivalently, this is satisfied if there exists a potential V such that the electric field $\boldsymbol{\mathscr{E}}$ can be obtained from its

gradient, i.e. $\mathscr{E} = -\nabla V$. That the potential $V(r, \theta)$ of Eq. (69) is indeed such a potential at all points including the boundary $\theta = \pi/2$, might not be immediately obvious since the force at the boundary is infinite involving a delta-function, i.e.

$$\begin{aligned}\mathbf{F}(r, \theta, \phi) &= -q\nabla V(r, \theta) \\ &= -q\hat{\mathbf{r}}u\left(\frac{\pi}{2} - \theta\right)\frac{\partial V(r)}{\partial r} \\ &\quad + q\frac{\hat{\boldsymbol{\theta}}}{r}\tilde{V}(r)\delta\left(\frac{\pi}{2} - \theta\right)\end{aligned} \tag{B.1}$$

However, it can be easily shown that the total energy is conserved in crossing the potential boundary by direct integration of the work W_{abcdefa} along an arbitrary closed path abcdefa (see Fig. 9) made up of two arcs of constant radius (r_1 and r_2) and two straight sections along the radial directions of constant θ ($\theta = \pi/2 \pm \theta_0$). The sharp boundary separating region I and II is at $\theta = \pi/2$. Thus, we have:

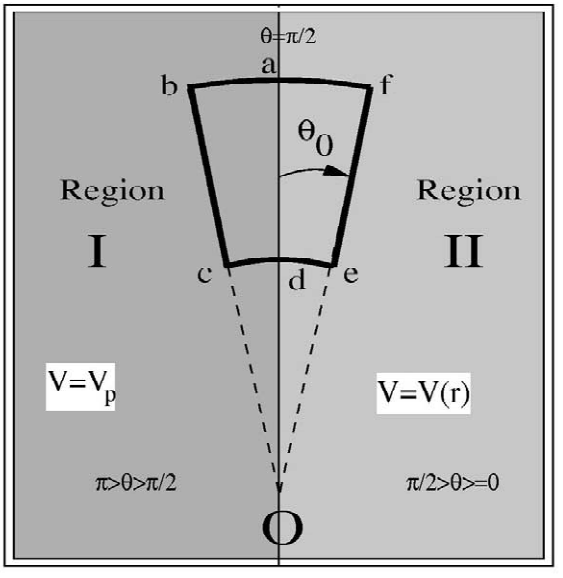

Fig. 9. Integration path (bold line) abcdefa used to show energy conservation across the potential step at $\theta = \pi/2$ (see text). The total work performed to go around the closed path abcdefa is zero. In Region I the potential is constant, while in Region II it is given by $V(r)$ of the analyser. $Oe = Od = Oc = r_1$ and $Of = Oa = Ob = r_2$ (see text). In this model, the potential boundary is sharp and the force at the boundary is infinite (delta-function).

$$W_{\text{abcdefa}} = \oint_{\text{abcdefa}} \mathbf{F}\cdot\mathrm{d}\mathbf{s} \tag{B.2}$$

$$= \int_{\text{c}}^{\text{e}} + \int_{\text{e}}^{\text{f}} + \int_{\text{f}}^{\text{b}} \mathbf{F}\cdot\mathrm{d}\mathbf{s} \tag{B.3}$$

with $W_{\text{bc}} = 0$ (force is zero) and

$$\begin{aligned}W_{\text{ce}} &= \int_{\text{c}}^{\text{e}} F_\theta r_1\,\mathrm{d}\theta \\ &= q\tilde{V}(r_1)\int_{\pi/2+\theta_0}^{\pi/2-\theta_0}\delta\left(\frac{\pi}{2} - \theta\right)\mathrm{d}\theta \\ &= -q\tilde{V}(r_1)\end{aligned} \tag{B.4}$$

similarly

$$\begin{aligned}W_{fb} &= \int_{f}^{b} F_\theta r_2\,\mathrm{d}\theta \\ &= q\tilde{V}(r_2)\int_{\pi/2-\theta_0}^{\pi/2+\theta_0}\delta\left(\frac{\pi}{2} - \theta\right)\mathrm{d}\theta \\ &= -q\tilde{V}(r_2)\end{aligned} \tag{B.5}$$

and finally

$$\begin{aligned}W_{\text{ef}} &= \int_{\text{e}}^{\text{f}} F_r\,\mathrm{d}r \\ &= -q\int_{r_1}^{r_2}\frac{\partial}{\partial r}V(r, \theta)\,\mathrm{d}r \\ &= -q\int_{r_1}^{r_2}\frac{\partial}{\partial r}V(r)\,\mathrm{d}r \\ &= -q[V(r_2) - V(r_1)] = -q[\tilde{V}(r_2) - \tilde{V}(r_1)]\end{aligned} \tag{B.6}$$

which when added up give $W_{\text{abcdefa}} = 0$. Any closed path joining regions I and II can always be represented by integrals of this type which cancel out. We shall use the potential $V(r, \theta)$ of Eq. (69) to compute the refraction of charged particles at the $\theta = \pi/2$ boundary.

B.2. Particle refraction across potential boundary (B.14)

The change in angular momentum in crossing the potential boundary is given by:

$$\frac{\mathrm{d}\mathbf{L}}{\mathrm{d}t} = \mathbf{r} \times \mathbf{F} \tag{B.7}$$

$$= -\mathbf{r} \times q\boldsymbol{\nabla} V(r, \theta)$$

$$= q\tilde{V}(r)\delta\left(\frac{\pi}{2} - \theta\right)(\hat{\mathbf{r}} \times \hat{\boldsymbol{\theta}}) \tag{B.8}$$

which shows that the change will be along the direction $\hat{\mathbf{r}} \times \hat{\boldsymbol{\theta}} \equiv \hat{\boldsymbol{\phi}} = -\sin\phi\hat{\mathbf{X}} + \cos\phi\hat{\mathbf{Y}}$ (see Fig. 3).

Taking the dot product of both sides of Eq. (B.8) with $\mathbf{L}$ and using the identity $\mathbf{L} \cdot (\hat{\mathbf{r}} \times \hat{\boldsymbol{\theta}}) = mr^2\dot{\theta}$ and $\frac{1}{2}d(\mathbf{L} \cdot \mathbf{L}) \equiv LdL$ we obtain:

$$\mathrm{d}(L^2) = 2mr^2 q\tilde{V}(r)\delta\left(\frac{\pi}{2} - \theta\right)\mathrm{d}\theta \tag{B.9}$$

This may be directly integrated in the *XYZ* frame along the path of the trajectory. Equivalently Eq. (B.9) maybe transformed to the plane of the trajectory by using the connection between the (r, θ, ϕ) and (r, ω) variables shown in Appendix C. From Eq. (C.13) we have $\cos\theta = \cos\beta\sin\omega$. Using the transformation of variables properties of delta-functions we have:

$$\delta\left(\frac{\pi}{2} - \theta\right)\mathrm{d}\theta = \sin\theta\delta(\cos\theta)\,\mathrm{d}\theta \tag{B.10}$$

$$= -\cos\beta\cos\omega\delta(\cos\beta\sin\omega)\,\mathrm{d}\omega \tag{B.11}$$

$$= -\delta(\omega)\,\mathrm{d}\omega \tag{B.12}$$

Then we may transform Eq. (B.9) to:

$$d(L^2) = -2mr^2 q\tilde{V}(r)\delta(\omega)\,\mathrm{d}\omega \tag{B.13}$$

Both Eqs. (B.9) and (B.13) can be directly integrated across the boundary $\theta = \pi/2$ or $\omega = 0$ from region I to region II along the trajectory to yield:

$$L^2 - L^{*2} = 2mq\int_{\pi/2^+}^{\pi/2^-} r(\theta)^2\tilde{V}(r(\theta))\delta\left(\frac{\pi}{2} - \theta\right)\mathrm{d}\theta$$

$$= -2mq\int_{0^-}^{0^+} r(\omega)^2\tilde{V}(r(\omega))\delta(\omega)\,\mathrm{d}\omega$$

$$= -2mr_0^2 q\tilde{V}(r_0)$$

At the entry radius $r = r_0$ the angular momenta must clearly be given by:

$$L^* = mr_0 v_0^* \sin\left(\frac{\pi}{2} + \alpha^*\right)$$

$$= r_0\sqrt{2mt}\cos\alpha^* \tag{B.15}$$

and

$$L = mr_0 v_0 \sin\left(\frac{\pi}{2} + \alpha\right)$$

$$= r_0\sqrt{2m\left(E + \frac{qk}{r_0}\right)}\cos\alpha$$

$$= r_0\sqrt{2m[t - q\tilde{V}(r_0)]}\cos\alpha \tag{B.16}$$

where v_0, v_0^* and α, α^* are the entry velocities and angles inside (region II) and outside (region I) the analyser.

Using Eqs. (B.14) and (B.15) we obtain:

$$L^2 = L^{*2}\left[1 - \frac{q\tilde{V}(r_0)}{t\cos^2\alpha^*}\right] \tag{B.17}$$

which expresses L in terms of the entry angle α^* (instead of α) and the potential $\tilde{V}(r_0)$.

From Eqs. (B.14)–(B.16) it is straightforward to show that:

$$v\sin\alpha = v^*\sin\alpha^* \tag{B.18}$$

$$v_r = v_r^* \tag{B.19}$$

$$v_\omega^2 - v_\omega^{*2} = -\frac{2q\tilde{V}(r_0)}{m} \tag{B.20}$$

and since $K = \frac{1}{2}mv^2 = \frac{1}{2}m(v_r^2 + v_\omega^2)$ and $t \equiv K^* = \frac{1}{2}mv^{*2}$ we may also write the change in kinetic energy ΔK^*, when crossing the boundary at r_0 as:

$$\Delta K^* \equiv K - K^* = -q\tilde{V}(r_0) \tag{B.21}$$

From Eq. (B.19) it is seen that the radial velocity, $v_r = \dot{r}$, is continuous across the boundary [6], as opposed to the angular velocity, $v_\omega = r\dot{\omega} = L/mr$ which is not. This has the consequence that since only the magnitude of L is discontinuous and not also its direction, the particle remains on the same plane as it crosses the potential boundary. Thus, the angle β, which defines the plane of the orbit will not

suffer any changes as the particle crosses the boundary. Eq. (B.18) is seen to be the charged-particle analog of Snell's law of refraction in optics [76].

Summarizing the relations between α and α^* we have:

$$\sin\alpha = \frac{v^*}{v}\sin\alpha^* = \frac{\sin\alpha^*}{\sqrt{1-\dfrac{q\tilde{V}(r_0)}{t}}} \tag{B.22}$$

$$\cos\alpha = \sqrt{\frac{1-\dfrac{q\tilde{V}(r_0)}{t\cos^2\alpha^*}}{1-\dfrac{q\tilde{V}(r_0)}{t}}}\cos\alpha^* \tag{B.23}$$

$$\tan\alpha = \frac{\tan\alpha^*}{\sqrt{1-\dfrac{q\tilde{V}(r_0)}{t\cos^2\alpha^*}}} = \frac{L^*}{L}\tan\alpha^* \tag{B.24}$$

It is evident from Eq. (B.22) that when $\tilde{V}(r_0)=0$ then $\alpha=\alpha^*$. The relation between α^* and α is shown in Fig. 10 for the case of paracentric entry with $\gamma=1.5$ and for conventional entry with $\gamma=1$. In both cases we have chosen the entry point, $r_0=R_0$. Clearly, the effect of refraction is non-negligible for paracentric entry and $\tilde{V}_0\neq 0$ ($\gamma\neq 1$).

We note that a similar refraction takes place at the exit of the HDA where the particle now crosses from region II back out to region I. Using the same treatment but applied at the exit point $\omega=\pi$ and r_π, Eqs. (B.14)–(B.24) can been seen to hold also when the subscript 0 indicating entry is substituted for π indicating exit. Now using Eq. (32), it can be readily shown that $\alpha_0^* = -\alpha_\pi^*$, *i.e. the particle's entry angle* $\alpha_0^*(\equiv\alpha^*)$ and exit angle α_π^* are equal to within a sign contrary to the relation between α_0 and α_π which are only equal if $r_0=r_\pi$ (see Eq. (32)).

In the majority of the literature treating HDAs the transition effects in crossing the potential boundaries at entry and exit have either been ignored, by treating the motion strictly inside the HDA or have been neglected. This primarily has to do with the fact that most treatments deal with conventional HDAs having $V_0=V_p$ and use very small slits or apertures with sizes typically ~ 0.5 mm or smaller so that $\tilde{V}(r_0)\approx\tilde{V}_0=0$ making $\alpha^*\approx\alpha$. This can be readily seen by expanding $\tilde{V}(r_0)$ in Eq. (B.22) around the entrance aperture at R_0 by setting $r_0=R_0+\Delta r_0$:

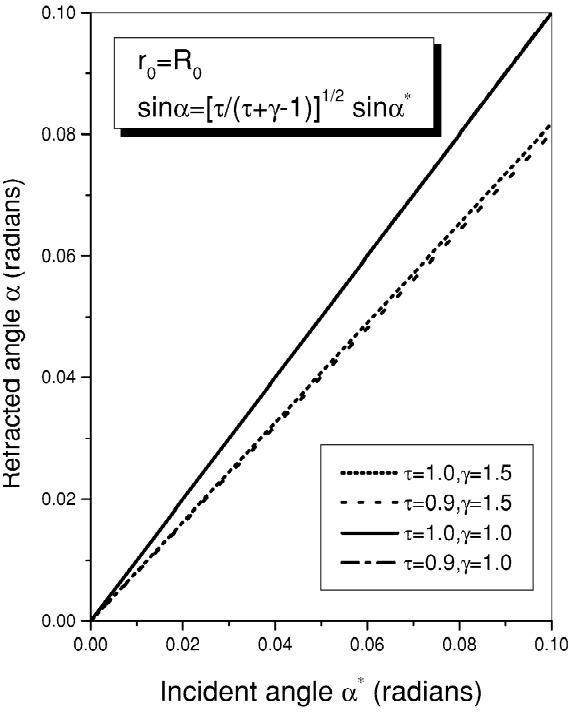

Fig. 10. Relation between the entry angle α^* prior to refraction (angle of incidence) and angle α after refraction (angle of refraction) for two cases: (a) $\gamma=1(\tilde{V}_0=0)$, $R_0=\bar{R}$, (b) $\gamma=1.5(\tilde{V}_0=0.5w)$, $R_0=82.55$ (paracentric entry). In both cases $q=-e$(electrons), $w=1000$ eV, $r_0=R_0$ and $R_\pi=\bar{R}$ with other parameters as given in Table 1. Clearly, the effect of refraction is non-negligible for paracentric entry and $\tilde{V}_0\neq 0$ ($\gamma\neq 1$).

$$\frac{\sin\alpha}{\sin\alpha^*} = \sqrt{1-\frac{q\tilde{V}(R_0+\Delta r_0)}{t}} = \left\{1+\frac{1}{2\tau}\left\{1-\gamma\left[1-\left(\frac{1}{\xi}+1\right)\frac{\Delta r_0}{R_0}\right]\right\}+\cdots\right\} \tag{B.25}$$

which for $\gamma=1$, $\xi=1$ gives:

$$\sin\alpha = \left(1+\frac{\Delta r_0}{\tau R_0}+\cdots\right)\sin\alpha^* \tag{B.26}$$

Clearly, $\Delta r_0/\tau R_0$ will always be very small since $\tau\approx 1$ and $\Delta r_0 << R_0$, especially for narrow slit spectrometers. However, when $\tilde{V}_0\neq 0$ ($\gamma\neq 1$) as for paracentric entry, even with $\Delta r_0=0$, the first order term will be important:

$$\sin\alpha \approx \left[1+\frac{1}{2\tau}(1-\gamma)\right]\sin\alpha^* \tag{B.27}$$

For example with $\gamma = 1.5$ and $\tau = 1$, Eq. (B.27) gives $\sin\alpha \approx 0.75 \sin\alpha^*$, a measurable effect. The exact relation is shown in Fig. 10 for some typical examples. In general, for $\gamma > 1$ we have $\alpha < \alpha^*$, while for $\gamma < 1$ we have $\alpha > \alpha^*$. As already discussed $\gamma > 1$ results in the acceleration of the particle right after entry which tends to minimize the spread in α. Smaller variation in α means smaller variation in the time-of-flight resulting in improved time resolution in coincidence measurements (e.g. e−2e measurements). Smaller variation in α also means smaller variation in the range of the trajectories implying decreased dispersion and larger energy acceptance window, as discussed in more detail in paper II.

Appendix C. Relation between (θ, ϕ) and ω in the $\omega_0 = 0$ coordinate system

As the particle moves along its trajectory on the orbital plane as a function of ω the corresponding spherical coordinate angles (θ, ϕ) must also change. The relation between the two sets of coordinates is derived here.

In the laboratory frame **XYZ** (see Fig. 3) we have:

$$\mathbf{r}(r,\theta,\phi) = r(\sin\theta\cos\phi\hat{\mathbf{X}} + \sin\theta\sin\phi\hat{\mathbf{Y}} + \cos\theta\hat{\mathbf{Z}}) \tag{C.1}$$

with the entry vector $\mathbf{r}_0$ given by:

$$\mathbf{r}_0 \equiv \mathbf{r}\left(r_0, \theta = \frac{\pi}{2}, \phi = \phi_0\right) \tag{C.2}$$

$$= r_0(\cos\phi_0\hat{\boldsymbol{X}} + \sin\phi_0\hat{\boldsymbol{Y}}) \tag{C.3}$$

Furthermore, it is readily seen from Fig. 3 that

$$\mathbf{v}_{0_{(x'y'z')}} = v_0(-\sin\alpha\hat{\mathbf{x}}' - \cos\alpha\sin\beta\hat{\mathbf{y}}' + \cos\alpha\cos\beta\hat{\mathbf{z}}') \tag{C.4}$$

which can be transformed to the *XYZ* system by a simple rotation around the common $\hat{\mathbf{Z}} = \hat{\mathbf{z}}'$ direction by the angle $\Phi_0 = \phi_0 - \pi$ (see Fig. 3):

$$\mathbf{v}_{0_{(XYZ)}} = \mathscr{R}(\Phi_0)\mathbf{v}_{0_{(x'y'z')}} \tag{C.5}$$

with

$$\mathscr{R}(\Phi_0) = \begin{pmatrix} \cos\Phi_0 & -\sin\Phi_0 & 0 \\ \sin\Phi_0 & \cos\Phi_0 & 0 \\ 0 & 0 & 1 \end{pmatrix} \tag{C.6}$$

This then gives:

$$\mathbf{v}_{0_{(XYZ)}} \equiv \mathbf{v}_0 = \times_0[(-\cos\alpha\sin\beta\sin\phi_0 + \sin\alpha\cos\phi_0)\hat{\mathbf{X}} + (\sin\alpha\sin\phi_0 + \cos\alpha\sin\beta\cos\phi_0)\hat{\mathbf{Y}} + \cos\alpha\cos\beta\hat{\mathbf{Z}}] \tag{C.7}$$

Given $\mathbf{r}_0$ and v_0 in the *XYZ* system we can easily compute the entry angular momentum $\mathbf{L}_0 = \mathbf{r}_0 \times v_0$ and $\mathbf{L}_0 \times \mathbf{r}_0$:

$$\mathbf{L}_0 = mr_0v_0\cos\alpha(\cos\beta\sin\phi_0\hat{\mathbf{X}} - \cos\beta\cos\phi_0\hat{\mathbf{Y}} + \sin\beta\hat{\mathbf{Z}}) \tag{C.8}$$

$$\mathbf{L}_0 \times \mathbf{r}_0 = L_0r_0(-\sin\beta\sin\phi_0\hat{\mathbf{X}} + \sin\beta\cos\phi_0\hat{\mathbf{Y}} + \cos\beta\hat{\mathbf{Z}}) \tag{C.9}$$

In the orbital plane frame *xy* we have using Eq. (51):

$$\mathbf{r} = r\left(\frac{\mathbf{r}_0}{r_0}\cos\omega + \frac{\mathbf{L}_0 \times \mathbf{r}_0}{L_0r_0}\sin\omega\right) \tag{C.10}$$

Taking the dot product of $\mathbf{r}$ in either frame with each one of the *XYZ* unit vectors and equating we have:

$$\sin\theta\cos\phi = \cos\phi_0\cos\omega - \sin\phi_0\sin\beta\sin\omega \tag{C.11}$$

$$\sin\theta\sin\phi = \sin\phi_0\cos\omega + \cos\phi_0\sin\beta\sin\omega \tag{C.12}$$

$$\cos\theta = \cos\beta\sin\omega \tag{C.13}$$

Eliminating $\sin\theta$ from Eqs. (C.11) and (C.12) we obtain:

$$\tan\phi = \frac{\tan\phi_0 + \sin\beta\tan\omega}{1 - \sin\beta\tan\phi_0\tan\omega} \tag{C.14}$$

Thus, given ϕ_0 and β which are defined at entry, Eqs. (C.13) and (C.14) determine θ and ϕ, respectively, as a function of ω.

Finally, we can also compute the angular momentum $\mathbf{L}_0$ using Eq. (51). Directly from the definition of $\mathbf{L}_0 \equiv \mathbf{r}_0 \times m\dot{\mathbf{r}}_0$ we get:

$$\mathbf{L}_0 = mr_0^2\dot{\omega}(\cos\beta \sin\phi_0\hat{\mathbf{X}} - \cos\beta\cos\phi_0\hat{\mathbf{Y}} + \sin\beta\hat{\mathbf{Z}}) \quad \text{(C.15)}$$

from which it can be directly shown that

$$L_0 \equiv \sqrt{\mathbf{L}_0 \cdot \mathbf{L}_0} = mr_0^2\dot{\omega} \quad \text{(C.16)}$$

as expected for a central field where the motion is confined to a plane. Equating the different expressions for L_0 above we get:

$$L_0 = mr_0 v_0 \cos\alpha = mr_0^2\dot{\omega}$$

from which we directly obtain Eqs. (22) and (23):

$$r_0\dot{\omega} = v_0\cos\alpha$$

References

[1] E.P. Benis, T.J.M. Zouros, Nucl. Instrum. Meth. Phys. Res. Sect. A 440 (2000) 462.
[2] E. Purcell, Phys. Rev. 54 (1938) 818.
[3] C.P. Browne, D.S. Craig, R.M. Williamson, Rev. Sci. Instrum. 22 (1951) 952.
[4] C. Kuyatt, J.A. Simpson, Rev. Sci. Instrum. 38 (1967) 103.
[5] S. Kevan, Rev. Sci. Instrum. 54 (1983) 1441.
[6] F. Hadjarab, J. Erskine, J. Electr. Spectr. Rel. Phenom. 36 (1985) 227.
[7] S. Nishigaki, S. Kanai, Rev. Sci. Instrum. 57 (1986) 225.
[8] E.-J. Jeong, J. Erskine, Rev. Sci. Instrum. 60 (1989) 3139.
[9] P. Louette et al., J. Electr. Spectr. Rel. Phenom. 52 (1990) 867.
[10] P. Baltzer, B. Wannberg, M.C. Göthe, Rev. Sci. Instrum. 62 (1991) 643.
[11] D. Hu, K. Leung, Rev. Sci. Instrum. 66 (1995) 2865.
[12] D.A. Dahl, SIMION 3D v6.0, Idaho National Engineering Laboratory, Idaho Falls, 1996.
[13] R. Herzog, Z. Phys. 97 (1935) 596.
[14] H. Wollnik, H. Ewald, Nucl. Instrum. Meth. 36 (1965) 93.
[15] U. Czok, K. Euler, M. Rauscher, H. Wollnik, Nucl. Instrum. Meth. 92 (1971) 365.
[16] H. Matsuda, Nucl. Instrum. Meth. 91 (1971) 637.
[17] A. Sköllermo, B. Wannberg, Nucl. Instrum. Meth. 131 (1975) 279.
[18] J.N.H. Brunt, F.H. Read, G.C. King, J. Phys. E: Sci. Instrum. 10 (1976) 134.
[19] K. Jost, J. Phys. E: Sci. Instrum. 12 (1979) 1001.
[20] K. Jost, J. Phys. E: Sci. Instrum. 12 (1979) 1006.
[21] C. Oshima, R. Franchy, H. Ibach, Rev. Sci. Instrum. 54 (1983) 1042.
[22] H. Wollnik (Ed.), Optics of Charged Particles, Academic Press, London, 1987, pp. pp. 1–291.
[23] B. Gurney, W. Ho, L.J. Richter, J. Villarrubia, Rev. Sci. Instrum. 59 (1988) 22.
[24] J. Osterwalder et al., J. Electr. Spectr. Rel. Phenom. 48 (1989) 55.
[25] A. Baraldi, V.R. Dhanak, G.C. King, Meas. Sci. Technol. 3 (1992) 778.
[26] P.W. Lorraine, B.D. Thoms, W. Ho, Rev. Sci. Instrum. 63 (1992) 1652.
[27] E.P. Benis et al., Nucl. Instrum. Meth. Phys. Res. Sect. B 146 (1998) 120.
[28] E.P. Benis, T.J.M. Zouros, P. Richard, Nucl. Instrum. Meth. Phys. Res. B 154 (1999) 276.
[29] E.P. Benis, T.J.M. Zouros, H. Aliabadi, P. Richard, Phys. Scripta T80B (1999) 529.
[30] T.J.M. Zouros, D.H. Lee, in: S.M. Shafroth, J.C. Austin (Eds.), Accelerator-based atomic physics techniques and applications, American Institute of Physics Conference Series, New York, 1997, pp. 426–79.
[31] T.J.M. Zouros, E.P. Benis, J.E. Schauer, in: J.L. Duggan, I.L. Morgan (Eds.), Application of Accelerators in Research and Industry, American Institute of Physics, AIP Conference Proceedings, New York, 2001, Vol. 576, pp. 76–79.
[32] D. Roy, J.-D. Carette, Can. J. Phys. 49 (1971) 2138.
[33] J.E. Draper, G.A. Ulloa, Nucl. Instrum. Meth. 157 (1978) 315.
[34] E.P. Benis, T.J.M. Zouros, J. Electr. Spectr. Rel. Phenom. (2002).
[35] T.J.M. Zouros, E. Benis, J. Electr. Spectr. Rel. Phenom. (2002).
[36] Y. Ballu, Revue de Physique Appliquée 3 (1968) 46.
[37] E.S.V.P. Afanas'ev, S.Y. Yavor, Sov. Phys. Tech. Phys. 18 (1974) 1072, [Translation of Zh. Tekh. Fiz. 43, 1703–7 (1973)].
[38] H. Polaschegg, Appl. Phys. 4 (1974) 63.
[39] B. Wannberg, A. Sköllermo, J. Electr. Spectr. Rel. Phenom. 10 (1977) 45.
[40] D. Dubé, D. Roy, Y. Ballu, Rev. Sci. Instrum. 52 (1981) 1497.
[41] M. Minkov, Sov. Phys. Tech. Phys. 5 (1971) 1285.
[42] L.M. Chase, Rev. Sci. Instrum. 44 (1973) 998.
[43] F. Paolini, G. Theodoridis, Rev. Sci. Instrum. 38 (1967) 579.
[44] G. Theodoridis, F. Paolini, Rev. Sci. Instrum. 40 (1969) 621.
[45] V. Afanas'ev, S.Y. Yavor, Sov. Phys. Tech. Phys. 20 (1975) 296, [Translation of Zh. Tekh. Fiz. 45, 471–80 (1975)].
[46] H. Goldstein, Classical Mechanics, Addison–Wesley, Reading, Massachussets, 1965.
[47] D.L. Landau, E.M. Lifschitz, Mechanics, Pergamon Press, Addison–Wesley Publishing Company, Reading, Massachusetts, 1969.
[48] V. Barger, M. Olsson, Classical Mechanics: A Modern Perspective, 2nd Edition, McGraw–Hill Inc, New York, 1995.
[49] J.E. Prussing, B.A. Conway, Orbital Mechanics, Oxford University Press, Oxford, 1993.

[50] D. Roy, D. Tremblay, Rep. Progr. Phys. 53 (1990) 1621.
[51] V. Schmidt, Electron Spectrometry of Atoms using Synchrotron Radiation, Cambridge, Cambridge, 1997.
[52] H. Wollnik, Nucl. Instrum. Meth. 52 (1967) 250.
[53] C.E. Kuyatt, in: B. Bederson, W.L. Fite (Eds.), Methods of Experimental Physics, Atomic and Electron Physics—Atomic Interactions, Vol. 7A, Academic Press, New York, 1968, pp. 1–43.
[54] D. Roy, J. Carette, in: H. Ibach (Ed.), Electron Spectroscopy For Surface Analysis, Springer–Verlag, Berlin, 1977, pp. 13–58.
[55] V.P. Afanas'ev, S.Y. Yavor, Sov. Phys. Tech. Phys. 20 (1976) 715, [Translation of Zh. Tekh. Fiz. 45, 1137–70 (1975)].
[56] D. Roy, J. Carette, in: H. Ibach (Ed.), Electron Spectroscopy For Surface Analysis, Springer–Verlag, Berlin, 1977, pp. 13–58.
[57] Y. Ballu, in: A. Septier (Ed.), Applied Charged Particle Optics, Vol. Part B, Academic, New York, 1980, pp. 257–381.
[58] D. Heddle, J. Phys. E: Sci. Instrum. 4 (1971) 589.
[59] P. Kemeny et al., Rev. Sci. Instrum. 44 (1973) 1197.
[60] D. Roy, J.-D. Carette, Appl. Phys. Lett. 16 (1970) 413.
[61] H. Wollnik, in: A. Septier (Ed.), Focusing of Charged Particles, Vol. II, Academic Press, New York, 1967, pp. 163–201.
[62] A. Poulin, D. Roy, J. Phys. E: Sci. Instrum. 11 (1978) 35.
[63] H. Polaschegg, Appl. Phys. 9 (1976) 223.
[64] R.E. Imhof, A. Adams, G. King, J. Phys. E: Sci. Instrum. 9 (1976) 138.
[65] L. Boesten, J. Phys. E: Sci. Instrum. 18 (1985) 232.
[66] A. Mann, F. Linder, J. Phys. E: Sci. Instrum. 21 (1988) 805.
[67] A. Baraldi, V.R. Dhanak, J. Electr. Spectr. Rel. Phenom. 67 (1994) 211.
[68] S.C. Page, F.H. Read, Nucl. Instrum. Meth. Phys. Res. Sect. A 363 (1995) 249.
[69] K. Siegbahn et al., ESCA—Atomic, Molecular and Solid State Structure Studied by Means of Electron Spectroscopy, Vol. 20, Almqvist and Wiksell, Uppsala, 1967.
[70] V.D. Belov, M.I. Yavor, Rev. Sci. Instrum. 71 (2000) 1651.
[71] F. Mariani, Rev. Sci. Instrum. 41 (1970) 807.
[72] H. Ewald, H. Liebl, Z. Naturforsch. 10a (1955) 872.
[73] R. Albrecht, Z. Naturforsch. 11a (1956) 156.
[74] V. Barger, M. Olsson, Classical Mechanics: A Modern Perspective, 1st Edition, McGraw–Hill, New York, 1973.
[75] E.A. Solov'ev, Sov. Phys. JETP 55 (1982) 1017.
[76] J.H. Moore, C.C. Davis, M.A. Coplan, Building Scientific Apparatus, Addison–Wesley, London, 1983.
[77] B. Sulik, N. Stolterfoht, in: S.M. Shafroth, J.C. Austin, Accelerator-Based Atomic Physics Techniques and Applications, American Institute of Physics Conference Series, New York, 1997, pp. 377–425.
[78] D.H. Lee et al., Nucl. Instrum. Meth. Phys. Res. B 40/41 (1989) 1229.